

RESEARCH ARTICLE | MARCH 20 2024

## An interface tracking, finite volume code for modeling axisymmetric implosion of a rotating liquid metal liner with free surface

Ivan V. Khalzov  ; Daymon Krotez  ; Raphaël Ségas 



*Physics of Fluids* 36, 032125 (2024)

<https://doi.org/10.1063/5.0196467>



View  
Online



Export  
Citation

### Articles You May Be Interested In

Explosion formation of high-velocity aluminum particles using combined shaped-charge liners

*AIP Conf. Proc.* (July 2023)

On the structure of plasma liners for plasma jet induced magnetoinertial fusion

*Phys. Plasmas* (February 2013)

Simulation study of the influence of experimental variations on the structure and quality of plasma liners

*Phys. Plasmas* (March 2019)

# An interface tracking, finite volume code for modeling axisymmetric implosion of a rotating liquid metal liner with free surface

Cite as: Phys. Fluids **36**, 032125 (2024); doi: [10.1063/5.0196467](https://doi.org/10.1063/5.0196467)

Submitted: 7 January 2024 · Accepted: 27 February 2024 ·

Published Online: 20 March 2024



View Online



Export Citation



CrossMark

Ivan V. Khalzov, Daymon Krotez, and Raphaël Ségas<sup>a)</sup>

## AFFILIATIONS

General Fusion Inc., 6020 Russ Baker Way, Richmond, British Columbia V7B 1B4, Canada

<sup>a)</sup>Author to whom correspondence should be addressed: [raphael.segas@generalfusion.com](mailto:raphael.segas@generalfusion.com)

## ABSTRACT

We present Integrated System Model-hydrodynamics (ISM-hydro)—an interface tracking, finite volume code for modeling a shaped implosion of a rotating, initially cylindrical, fluid shell (liner) with a free surface. The code is a novel implementation of the mixed Lagrangian–Eulerian approach, applied to a compressible fluid in an axisymmetric geometry described by cylindrical coordinates  $(r, \phi, z)$ . In ISM-hydro, a structured quadrilateral mesh follows fluid elements in the  $r$ -direction (radially Lagrangian) and is fixed in the  $z$ -direction (axially Eulerian). This approach accurately captures the motion of the liner’s free surface, making it an interface tracking method. Using this mesh, we derive a finite volume discretization of the axisymmetric Euler equations for a rotating compressible fluid that has an exact balance of kinetic energy. An extensive comparison between ISM-hydro and the open-source software OpenFOAM is presented; results for different test cases show very good agreement in simulated implosion trajectories and flow fields. ISM-hydro is the purely hydrodynamic component of the Integrated System Model (ISM), a framework developed at General Fusion (GF) for comprehensive predictive modeling of GF’s magnetized target fusion (MTF) scheme, where an imploding rotating liquid metal liner compresses a magnetized plasma target to fusion conditions. Among advantages of the code is its speed: a full implosion simulation with a coarse mesh takes on the order of one minute on a single core while preserving high accuracy. This makes ISM-hydro a valuable tool for the design optimization of GF’s MTF machines.

© 2024 Author(s). All article content, except where otherwise noted, is licensed under a Creative Commons Attribution (CC BY) license (<https://creativecommons.org/licenses/by/4.0/>). <https://doi.org/10.1063/5.0196467>

## I. INTRODUCTION

The goal of this paper is to present the Integrated System Model-hydrodynamics (ISM-hydro) code developed at General Fusion (GF) as part of the Integrated System Model (ISM) framework. The ultimate objective of the ISM is to provide predictive and complete simulations of the magnetized target fusion (MTF) systems being designed at GF.<sup>1</sup> GF’s MTF concept is illustrated in Fig. 1. A magnetized plasma (target) is injected into an initially cylindrical cavity formed inside a liquid metal shell (liner) contained in a rotating vessel (rotor). A pneumatic driving system generates carefully tuned pressures that push on the liner’s outer surface nonuniformly, causing the liner to implode and change in shape (shaped implosion), thereby compressing the target to fusion conditions.

The development of ISM-hydro is motivated by the need for fast (on the order of one minute on a single core) and accurate simulations of the liner’s motion, especially the dynamics of its inner surface during implosion (implosion trajectory), which can then be used in GF’s

MTF system design optimization process. A number of simplifying assumptions are made in ISM-hydro. First, it is assumed that the liner’s motion is governed by pure hydrodynamics; in particular, the effects of magnetic fields and the plasma are neglected. This eliminates the complexity of fully coupled modeling of different parts of the MTF system with different time scales and physics, although GF has made good progress in this area.<sup>2</sup> Second, the liner is assumed to be axisymmetric and laminar throughout the implosion. This is justified by the results of the recent paper,<sup>3</sup> showing that axisymmetric laminar simulations of liquid liner implosions are in excellent agreement with experimental data, provided that the liner’s inner surface remains Rayleigh–Taylor stable. Third, the deformation (deviation from cylindricity) of the liner’s inner surface is assumed to be moderate and without topological changes. This greatly simplifies the simulation of the liner’s inner surface motion during implosion.

To accurately simulate the dynamics of the liner with free surface, ISM-hydro uses a mixed Lagrangian–Eulerian fluid description similar

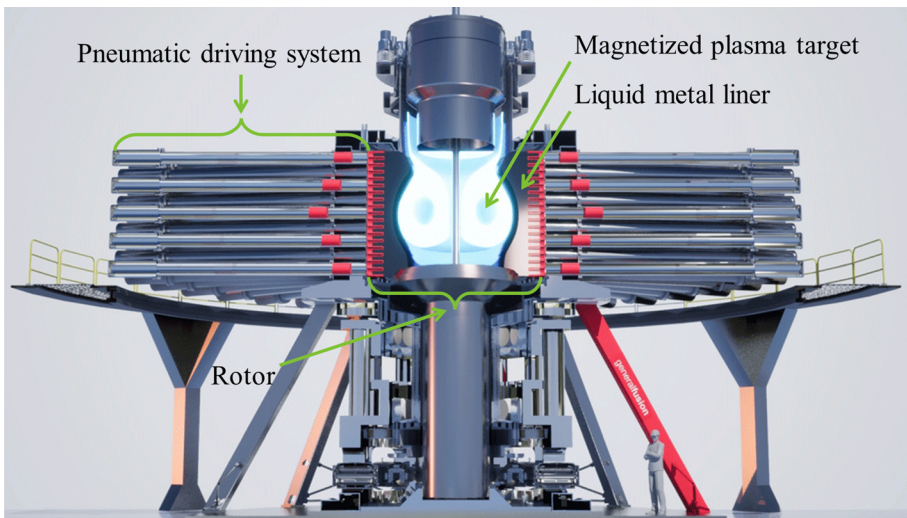


**FIG. 1.** GF's MTF concept: a magnetized plasma target is compressed to fusion conditions by a shaped implosion of a liquid metal liner.

to the so-called multilayer shallow water models, which are applicable to a wide range of problems from geophysical flow<sup>4,5</sup> to the movement of micro-organisms.<sup>6,7</sup> The description is based on dividing the fluid into multiple layers in the direction transverse to the free surface, and then following dynamics of their boundaries in a Lagrangian way, while treating the flows within each layer in an Eulerian way. This approach naturally tracks the motion of the fluid's free surface, making it an interface tracking method.<sup>8,9</sup> Typical multilayer shallow water models consider an incompressible fluid (water) in a vertical gravity field with a free surface close to horizontal, so the Lagrangian direction is vertical. The pressure distribution within such a fluid is approximately hydrostatic, assuming separation of horizontal and vertical length scales (shallow water assumption). ISM-hydro, on the contrary, describes a rotating compressible fluid in axisymmetric geometry with a free surface close to cylindrical, so the Lagrangian direction in this case is radial. The fluid pressure distribution is given by the corresponding equation of state, and no assumptions about length scales of the problem are made (no shallow water assumption). Implementation of these elements in combination with the mixed Lagrangian–Eulerian approach represents a novelty of the ISM-hydro scheme. Note that for such a scheme to be functional, the assumption of moderate deformations without topological changes should also hold for all fluid layers. The advantages of the mixed Lagrangian–Eulerian approach are the absence of fluid advection between layers and the possibility of using a structured quadrilateral mesh. In the ISM-hydro scheme, this leads to a simplified finite volume discretization of the axisymmetric Euler equations for a compressible rotating fluid which has an exact balance of kinetic energy, a property usually not satisfied in other finite volume algorithms.

ISM-hydro is intended to predict liner implosions accurately and efficiently while enabling coupling with other relevant components, such as plasma and pneumatic drive models, as part of the ISM framework. This framework is meant to support the development and design of GF's MTF systems and, ultimately, viable fusion power generation by facilitating comprehensive design optimization processes and analysis of experimental results.

The rest of the paper is organized as follows. Section II describes the numerical method used in ISM-hydro. Section III presents a convergence study and a comparison of high-resolution simulation results between ISM-hydro and the open-source software OpenFOAM. Section IV summarizes the advantages and limitations of our method.

## II. ISM-HYDRO NUMERICAL METHOD

### A. Problem statement

In order to present the details of our numerical method, we consider a simplified axisymmetric model of the MTF system being pursued by GF. Gravity, surface tension, and shear viscosity are neglected, although we acknowledge they can play a role in the liner dynamics. Figure 2 displays the geometry of the model in the  $r$ - $z$  plane in cylindrical coordinates  $(r, \phi, z)$ . By convention, the axis of revolution is located at  $r = 0$  and the equatorial plane at  $z = 0$ . The rotor is a cylinder with outer radius  $R_b$  and height  $H$ . The rotor's top and bottom plates, located at  $z = H/2$  and  $z = -H/2$ , are referred to as the end plates. The rotor contains  $N_c$  distinct horizontal channels (annular slots), which are uniformly distributed along the axial direction and extend radially from  $R_a$  to  $R_b$ . The channels are separated by horizontal annular baffles of non-zero uniform thickness [horizontal gray bands in Figs. 2(a) and 2(b)]; these baffles are a simplified representation of the rotor structure illustrated in Fig. 1.

As shown in Fig. 2(a), at time  $t = 0$ , the liquid liner (red region) undergoes solid body rotation at angular velocity  $\omega|_{t=0} = \Omega_0$ . Due to centrifugal forces, the spinning liquid completely fills the rotor channels and forms a cylindrical cavity of radius  $R_0$  occupied with an ideal gas of low pressure  $p_0$ .

Implosion of the liner is initiated by applying time-varying driving gas pressures  $P_i(t)$  to each channel inlet at  $r = R_b$  (corresponding to the initial outer radius of the liner), where  $i = 1, \dots, N_c$  is the numbering of the channels from bottom to top as shown in Fig. 2(b). Functions  $P_i(t)$  represent the pressures generated by the pneumatic driving system. For the test cases considered in Sec. III, these functions are given in a simple analytical form. Note that the driving pressures can vary from channel to channel; this is how shaped implosion is achieved. As time progresses and the liner moves radially inward, the driving pressures

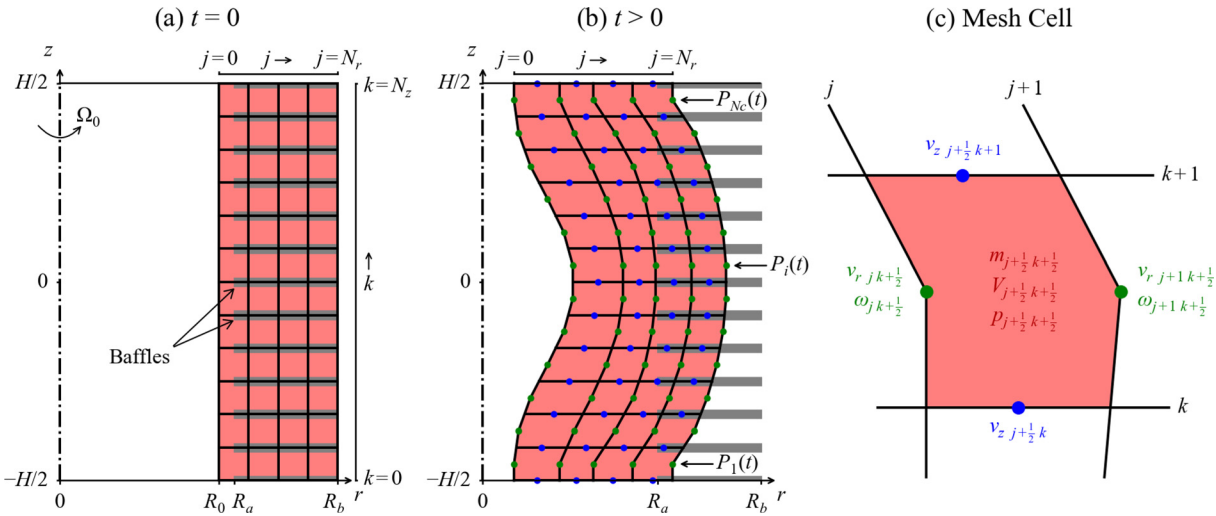


**FIG. 2.** Geometry and numerical mesh of the ISM-hydro model for a case where the number of horizontal mesh layers is equal to the number of rotor channels,  $N_z = N_c$ . (a) At time  $t = 0$ , the liquid liner (red), spinning together with the rotor (of height  $H$  and radius  $R_b$ ), fills the rotor channels (separated by gray horizontal baffles extending radially from  $R_a$  to  $R_b$ ) and forms a cylindrical cavity of radius  $R_0$ . (b) At later time  $t > 0$ , due to applied driving pressures  $P_i(t)$ , the liner implodes radially and changes in shape; the numerical mesh follows the liner's motion. (c) A zoomed mesh cell showing the staggering of physical quantities in our finite volume scheme.

continue to be applied at the liner's outer surface; this assumes that the driving gas pressure equilibrates instantly inside each channel.

## B. Finite volume discretization

Here, we describe the finite volume method implemented in ISM-hydro for simulating a compressible axisymmetric liquid metal liner. The advantage of finite volume discretization over other methods is that it naturally preserves the conservative form of the original Euler equations. These equations in cylindrical coordinates are the continuity equation and the three components of the axisymmetric inviscid momentum equation, namely,

$$\dot{\rho} = -\nabla \cdot (\rho \mathbf{v}), \quad (1a)$$

$$(\rho v_r)' = -\nabla \cdot (\rho v_r \mathbf{v}) + \rho \omega^2 r - p'_r, \quad (1b)$$

$$(\rho v_z)' = -\nabla \cdot (\rho v_z \mathbf{v}) - p'_z, \quad (1c)$$

$$(\rho \omega r^2)' = -\nabla \cdot (\rho \omega r^2 \mathbf{v}), \quad (1d)$$

where  $\rho$  is the density,  $\mathbf{v}$  is the velocity vector containing only radial  $v_r$  and axial  $v_z$  components,  $\omega$  is the angular velocity, and  $p$  is the pressure. Here and below, a dot above a quantity corresponds to a partial derivative of this quantity with respect to time, and a prime denotes a partial derivative with respect to the coordinate indicated in the subscript.

For finite volume discretization of system (1), we introduce a structured quadrilateral mesh in the  $r$ - $z$  plane as depicted in Fig. 2. Namely, at time  $t = 0$ , the cylindrical liquid liner is divided in the radial direction into  $N_r$  vertical layers of equal thickness  $\Delta r_0$ , separated by vertical mesh lines

$$r_j|_{t=0} = R_0 + j\Delta r_0, \quad \Delta r_0 = \frac{R_b - R_0}{N_r}, \quad j = 0, \dots, N_r. \quad (2)$$

During the implosion, the vertical mesh lines are advected with the fluid flow and can deform (Lagrangian description). They do not remain vertical in general,

$$r_j = r_j(t, z), \quad j = 0, \dots, N_r, \quad (3)$$

where functions  $r_0(t, z)$  and  $r_{N_r}(t, z)$  describe the shape of the liner's inner and outer free surfaces for all times  $t$ , respectively. Due to their Lagrangian definition, the vertical mesh lines  $r_j$  in Eq. (3) are treated as impenetrable boundaries (i.e., no flow is allowed across them and the mass of each vertical layer is conserved). In Sec. III C, we also introduce radially non-uniform initial meshes by further subdividing the innermost vertical layer in Eq. (2). In the axial direction, the liquid liner is divided into  $N_z$  equal horizontal layers of thickness  $\Delta z$  with fixed boundaries (horizontal mesh lines) given by

$$z_k = -\frac{H}{2} + k\Delta z, \quad \Delta z = \frac{H}{N_z}, \quad k = 0, \dots, N_z. \quad (4)$$

The presence of baffles in the geometry restricts the choice for the number of horizontal mesh layers  $N_z$ ; specifically, it can only be a multiple of the number of rotor channels  $N_c$

$$N_z = K_c N_c,$$

where the integer  $K_c$  is the number of horizontal mesh layers per channel. In this case, the horizontal mesh lines from Eq. (4) with indices  $k = 0, K_c, 2K_c, \dots, N_c K_c$  correspond to the midplanes of the baffles. In the following discussion, we reserve notation  $i$  for numbering of the rotor channels, and  $j$  and  $k$  for radial and axial indices of the mesh nodes, respectively.

We apply a staggered-grid arrangement of quantities, a standard practice for finite volume methods. Velocity components  $v_r$  and  $v_z$  are defined at the faces of the mesh cells [indices  $(j, k + 1/2)$  and  $(j + 1/2, k)$ , respectively], while density  $\rho$  and pressure  $p$  are defined at the cell centers [indices  $(j + 1/2, k + 1/2)$ ], as shown in Fig. 2(c). We also define the discretized angular velocity  $\omega$  at the same faces as the radial velocity  $v_r$  [indices  $(j, k + 1/2)$ ]. The control volumes for each of these discretized quantities are defined in the  $j$ - $k$  index plane as unit squares centered around the indices corresponding to the

quantity. For the density  $\rho$  and pressure  $p$ , the control volume coincides with the mesh cell. For the radial velocity  $v_r$  and angular velocity  $\omega$ , the control volume is bounded by the mesh lines  $r_{j-1/2}$ ,  $r_{j+1/2}$ ,  $z_k$ , and  $z_{k+1}$ . Similarly, the control volume for the axial velocity  $v_z$  is bounded by the mesh lines  $r_j$ ,  $r_{j+1}$ ,  $z_{k-1/2}$ , and  $z_{k+1/2}$ . Mesh lines with half-integer indices are defined as

$$r_{j+\frac{1}{2}}^2 = \frac{1}{2} (r_j^2 + r_{j+1}^2), \quad z_{k+\frac{1}{2}} = \frac{1}{2} (z_k + z_{k+1}).$$

Note that the control volumes are moving and changing in size and shape due to motion of the vertical mesh lines in the physical  $r$ - $z$  plane. For now, we consider the most general form of the discrete equations with no baffles. The effects of the baffles (reduction of cell volumes and zeroing of the axial velocity) are discussed at the end of this section.

Discretizing system (1) on the relevant control volumes, we obtain (details of this derivation are presented in Appendix A)

$$\dot{m}_{j+\frac{1}{2}k+\frac{1}{2}} = q_{j+\frac{1}{2}k}^m - q_{j+\frac{1}{2}k+1}^m, \quad (5a)$$

$$\dot{M}_{rjk+\frac{1}{2}} = q_{jk}^{M_r} - q_{jk+1}^{M_r} + m_{jk+\frac{1}{2}} \omega_{jk+\frac{1}{2}}^2 r_{jk+\frac{1}{2}} + f_{rjk+\frac{1}{2}}^p, \quad (5b)$$

$$\dot{M}_{zj+\frac{1}{2}k} = q_{j+\frac{1}{2}k-\frac{1}{2}}^{M_z} - q_{j+\frac{1}{2}k+\frac{1}{2}}^{M_z} + f_{zj+\frac{1}{2}k}^p, \quad (5c)$$

$$\dot{L}_{jk+\frac{1}{2}} = q_{jk}^L - q_{jk+1}^L. \quad (5d)$$

Quantities on the left-hand side (LHS) of system (5) are the corresponding control volume integrals of the LHS quantities of system (1), namely, the cell mass

$$\int_{V_{j+\frac{1}{2}k+\frac{1}{2}}} \rho dV \Rightarrow m_{j+\frac{1}{2}k+\frac{1}{2}} = \rho_{j+\frac{1}{2}k+\frac{1}{2}} V_{j+\frac{1}{2}k+\frac{1}{2}}, \quad (6)$$

the radial momentum

$$\int_{V_{j+\frac{1}{2}k}} \rho v_r dV \Rightarrow M_{rjk+\frac{1}{2}} = m_{jk+\frac{1}{2}} v_{rjk+\frac{1}{2}}, \quad (7)$$

the axial momentum

$$\int_{V_{j+\frac{1}{2}k}} \rho v_z dV \Rightarrow M_{zj+\frac{1}{2}k} = m_{j+\frac{1}{2}k} v_{zj+\frac{1}{2}k}, \quad (8)$$

and the angular momentum

$$\int_{V_{j+\frac{1}{2}k}} \rho \omega r^2 dV \Rightarrow L_{jk+\frac{1}{2}} = m_{jk+\frac{1}{2}} \omega_{jk+\frac{1}{2}} r_{jk+\frac{1}{2}}^2. \quad (9)$$

Here and below, the arrow denotes the discretization operation: the quantity at the tip of the arrow is the discrete approximation of the quantity at the base of the arrow.

We can already make several conclusions about the order of accuracy of our numerical scheme. If we introduce the coordinate  $x = r^2$ , then for any sufficiently smooth function  $f(x, z)$ , the integral over a control volume centered around some point  $(x_c, z_c)$  and bounded by mesh lines  $x_l(z)$ ,  $x_r(z)$ ,  $z_c - \Delta z/2$ ,  $z_c + \Delta z/2$  can be approximated using its Taylor expansion

$$\begin{aligned} \int_{V_c} f dV &= \pi \int_{z_c - \frac{\Delta z}{2}}^{z_c + \frac{\Delta z}{2}} \int_{x_l(z)}^{x_r(z)} f(x, z) dx dz \\ &= \pi \Delta x \Delta z \left( f_c + \frac{1}{2} f'_{x_c} (\Delta x_r - \Delta x_l) + \mathcal{O}(\Delta x^2, \Delta z^2) \right), \end{aligned} \quad (10)$$

where  $\Delta x_r = x_r(z_c) - x_c$ ,  $\Delta x_l = x_c - x_l(z_c)$ ,  $\Delta x = x_r(z_c) - x_l(z_c)$ , and subscript  $c$  means that function  $f$  and its derivative  $f'_x$  are taken at point  $(x_c, z_c)$ . From Eq. (10), it follows that approximations (6)–(9) are second order accurate in  $\Delta z$ ; this is due to the mesh uniformity in the axial direction. In general, the second order accuracy in  $\Delta z$  holds in the bulk of fluid domain for all terms introduced in the scheme later, but it reduces to the first order near the end plates for the radial velocity shear term (26). Equation (10) also shows that for general non-uniform meshes in  $x = r^2$  (i.e., when  $\Delta x_r \neq \Delta x_l$ , which is always the case for control volumes at the fluid surface), the scheme has only the first order accuracy in  $\Delta x$  (or, equivalently, in  $\Delta r_0$ ). Therefore, we expect the ISM-hydro numerical scheme to be first order accurate in both  $\Delta r_0$  and  $\Delta z$ . We note that such accuracy is satisfactory for our primary purpose of simulating the liner's inner surface dynamics (implosion trajectory), although it can lead to smearing of possible shocks inside the liner.

Choosing  $f = 1$  in Eq. (10), we obtain an approximation for the cell volume entering Eq. (6),

$$\int_{V_{j+\frac{1}{2}k+\frac{1}{2}}} dV \Rightarrow V_{j+\frac{1}{2}k+\frac{1}{2}} = \pi \Delta z \left( r_{j+1k+\frac{1}{2}}^2 - r_{jk+\frac{1}{2}}^2 \right), \quad (11)$$

which is accurate to the second order in  $\Delta z$ . The control volume masses entering Eqs. (7)–(9) are defined as averages between two corresponding cell masses

$$m_{jk+\frac{1}{2}} = \frac{1}{2} (m_{j-\frac{1}{2}k+\frac{1}{2}} + m_{j+\frac{1}{2}k+\frac{1}{2}}), \quad (12a)$$

$$m_{j+\frac{1}{2}k} = \frac{1}{2} (m_{j+\frac{1}{2}k-\frac{1}{2}} + m_{j+\frac{1}{2}k+\frac{1}{2}}). \quad (12b)$$

At the fluid domain boundary, these masses are simply halves of the masses of the corresponding boundary cells. For example, at the liner's inner ( $j = 0$ ) and outer ( $j = N_r$ ) surfaces, we have

$$m_{0k-\frac{1}{2}} = \frac{1}{2} m_{\frac{1}{2}k-\frac{1}{2}}, \quad m_{N_r k-\frac{1}{2}} = \frac{1}{2} m_{N_r-\frac{1}{2}k-\frac{1}{2}}, \quad k = 1, \dots, N_z. \quad (13)$$

The fluid radial velocity in Eq. (7) is determined by the full time derivative of the radial position of the vertical mesh line  $r_j$ , as follows from its Lagrangian nature

$$v_{rj} \equiv \frac{dr_j(t, z(t))}{dt} = \dot{r}_j + (r_j)'_z v_{zj}, \quad (14)$$

where the last term is due to the shear of the vertical mesh line  $r_j$ . In general, we can rewrite Eq. (14) for all indices as

$$v_{rjk+\frac{1}{2}} = \dot{r}_{jk+\frac{1}{2}} + \delta v_{rjk+\frac{1}{2}}, \quad (15)$$

where the discrete form of the shear term  $\delta v_{rjk+\frac{1}{2}}$  is specified later in this section [see Eq. (26)]. The primary variables in our numerical scheme are  $m_{j+1/2k+1/2}$ ,  $r_{jk+1/2}$ ,  $\dot{r}_{jk+1/2}$ ,  $v_{zj+1/2k}$ , and  $\omega_{jk+1/2}$ . All other quantities are expressed using them.

The terms on the right-hand side (RHS) of system (5) represent the fluxes through the top and bottom faces of the control volumes, denoted as  $q$  with the corresponding quantity as a superscript, and the forces integrated over the control volumes: the centrifugal force,  $m\omega^2 r$ , acting in the radial direction, and the components of the pressure force,  $f_r^p$  and  $f_z^p$ , acting in the radial and axial directions, respectively. Note that there are no fluxes through the left and right faces of the control volumes because of the radially Lagrangian property. The definition of the pressure force components is

$$f_{rjk+\frac{1}{2}}^p = -(p_{j+\frac{1}{2}k+\frac{1}{2}} - p_{j-\frac{1}{2}k+\frac{1}{2}})S_{jk+\frac{1}{2}}, \quad (16a)$$

$$f_{zj+\frac{1}{2}k}^p = -(p_{j+\frac{1}{2}k+\frac{1}{2}} - p_{j+\frac{1}{2}k-\frac{1}{2}})S_{j+\frac{1}{2}k} + \delta f_{zj+\frac{1}{2}k}^p, \quad (16b)$$

with the vertical and horizontal area elements given by

$$S_{jk+\frac{1}{2}} = 2\pi r_{jk+\frac{1}{2}} \Delta z, \quad (17a)$$

$$S_{j+\frac{1}{2}k} = \pi(r_{j+1k}^2 - r_{jk}^2), \quad (17b)$$

and the radial position of each mesh node defined consistently with the rest of the scheme as

$$r_{jk}^2 = \frac{1}{2} \left( r_{jk-\frac{1}{2}}^2 + r_{jk+\frac{1}{2}}^2 \right). \quad (18)$$

The additional term in Eq. (16b) is due to the shear of the vertical mesh line  $r_{j+1/2}$  [its discrete form is given in Eq. (31)]. Indeed, a full  $z$ -derivative of pressure along the mesh line  $r_{j+1/2}$  (a derivative at fixed radial index  $j + 1/2$ ) is

$$\left( \frac{dp}{dz} \right)_{j+\frac{1}{2}} \equiv \frac{dp(r_{j+\frac{1}{2}}(t, z), z)}{dz} = p'_{zj+\frac{1}{2}} + (r_{j+\frac{1}{2}})' p'_{rj+\frac{1}{2}}, \quad (19)$$

where  $p'_{zj+1/2}$  is the partial  $z$ -derivative of pressure (a derivative at fixed radius  $r$ ) evaluated at a point with coordinates  $(r_{j+1/2}(t, z), z)$ . This is the partial  $z$ -derivative that enters Eq. (1c) and determines the axial pressure force through the control volume integral. So, using Eq. (19), the axial pressure force in Eq. (5c) can be decomposed as

$$f_{zj+\frac{1}{2}k}^p \Leftarrow - \int_{V_{j+\frac{1}{2}k}} p'_z dV = - \int_{V_{j+\frac{1}{2}k}} \left( \frac{dp}{dz} \right)_{j+\frac{1}{2}} dV + \int_{V_{j+\frac{1}{2}k}} (r_{j+\frac{1}{2}})' z p'_{rj+\frac{1}{2}} dV,$$

where the resulting two integrals correspond to the two terms in Eq. (16b).

To fully specify pressure forces in system (5), we need an expression for the fluid pressure in every mesh cell as a function of primary quantities. In ISM-hydro, we use the Cole (also known as modified Tait) equation of state (EOS),<sup>10</sup> relating the pressure to the local fluid density

$$p_{j+\frac{1}{2}k+\frac{1}{2}}^{EOS} = \begin{cases} \frac{\rho_0 c_s^2}{\Gamma} \left( \left( \frac{\rho_{j+\frac{1}{2}k+\frac{1}{2}}}{\rho_0} \right)^\Gamma - 1 \right) & \text{if } \rho_{j+\frac{1}{2}k+\frac{1}{2}} > \rho_0, \\ 0 & \text{otherwise,} \end{cases} \quad (20)$$

where  $\rho_0$  is the reference density,  $c_s$  is the sound speed, and  $\Gamma$  is the stiffness exponent (adiabatic index). No specific cavitation model is considered in the equation of state (20); any cells where the fluid density drops below the reference density behave as a fluid with zero pressure.

For stability of our numerical scheme, we introduce an artificial viscosity—a typical approach in staggered-grid Lagrangian methods, originally designed for problems containing shocks (see, for example, Refs. 11–13 and references therein). We choose a linear form of artificial viscosity (linear in fluid velocity gradient), which is analogous to bulk viscosity. Mathematically, it is expressed as an additional term in the cell fluid pressure

$$p_{j+\frac{1}{2}k+\frac{1}{2}} = p_{j+\frac{1}{2}k+\frac{1}{2}}^{EOS} - \nu \rho_{j+\frac{1}{2}k+\frac{1}{2}} (\nabla \cdot \mathbf{v})_{j+\frac{1}{2}k+\frac{1}{2}}, \quad (21)$$

where  $\nu$  is the artificial kinematic bulk viscosity, which is considered constant in the fluid domain, and the discrete divergence of the fluid velocity is given as (see Appendix A for details)

$$(\nabla \cdot \mathbf{v})_{j+\frac{1}{2}k+\frac{1}{2}} = \frac{\dot{r}_{j+1k+\frac{1}{2}} S_{j+1k+\frac{1}{2}} - \dot{r}_{jk+\frac{1}{2}} S_{jk+\frac{1}{2}} + v_{zj+\frac{1}{2}k+1} S_{j+\frac{1}{2}k+1} - v_{zj+\frac{1}{2}k} S_{j+\frac{1}{2}k}}{V_{j+\frac{1}{2}k+\frac{1}{2}}}. \quad (22)$$

This extra pressure component adds diffusion-like terms to the purely advective momentum equations (5b) and (5c), turning them into advection–diffusion equations. The optimal value of  $\nu$  for numerical stability is determined by the sound speed in the fluid and the initial radial cell size

$$\nu = C_L c_s \Delta r_0,$$

where  $C_L$  is a case specific non-dimensional coefficient, usually close to 0.5. Note that adding this artificial viscosity, linear in  $\Delta r_0$ , does not change the overall first order accuracy of the scheme and ensures convergence of the discrete equations to inviscid system (1) in the limit  $\Delta r_0 \rightarrow 0$ . We verified that the values of artificial viscosity provide numerical stability while having a negligible effect on implosion trajectories.

Since accurate simulation of possible shocks in the liner is not our primary focus, and an artificial viscosity is already explicitly introduced for stability of our scheme, we do not require any special (Godunov-type) representations of the face fluxes. Therefore, the mass flux in Eq. (5a) can be discretized directly as

$$\int_{r_{jk}}^{r_{j+1k}} (\rho v_z) \Big|_{z=z_k} 2\pi r dr \Rightarrow q_{j+\frac{1}{2}k}^m = \rho_{j+\frac{1}{2}k} v_{zj+\frac{1}{2}k} S_{j+\frac{1}{2}k} = \frac{m_{j+\frac{1}{2}k} v_{zj+\frac{1}{2}k}}{\Delta z}. \quad (23)$$

There is some freedom in discretizing the remaining face fluxes  $q$  in system (5) and shear terms in Eqs. (15) and (16b). We use this freedom to make our scheme satisfy additional properties inherent to continuous system (1). Specifically, we want to have the discrete analogues of the axial pressure force balance

$$\int_V p'_z dV = \int_{\partial V} p dS \quad (24)$$

(i.e., the axial pressure force is canceled inside the fluid volume) and the fluid kinetic energy balance

$$\frac{d}{dt} \int_V \frac{1}{2} \rho \mathbf{v}^2 dV = \int_V p (\nabla \cdot \mathbf{v}) dV - \int_{\partial V} p \mathbf{v} \cdot \mathbf{ds} \quad (25)$$

(i.e., the change of total kinetic energy is only due to the work done by pressure), where  $V$  is the entire fluid domain,  $\partial V$  is its boundary

surface, and  $d\mathbf{S} \equiv \mathbf{n} dS = (dS_r, dS_z)$  is the element of the surface area with unit normal vector pointing outward. The details of this derivation are outlined in [Appendix B](#). As a result, we obtain the following expression for the radial velocity shear term:

$$\delta v_{rjk+\frac{1}{2}} = \frac{v_{zjk+\frac{1}{2}}^t (r_{jk+1}^2 - r_{jk+\frac{1}{2}}^2) + v_{zjk+\frac{1}{2}}^b (r_{jk+\frac{1}{2}}^2 - r_{jk}^2)}{2\Delta z r_{jk+\frac{1}{2}}}. \quad (26)$$

Here, we introduce the mass averaged axial velocities at the top and bottom of the control volume ( $j, k + 1/2$ ),

$$v_{zjk+\frac{1}{2}}^t = w_{jk+\frac{1}{2}}^l v_{zj-\frac{1}{2}k+1} + w_{jk+\frac{1}{2}}^r v_{zj+\frac{1}{2}k+1}, \quad (27a)$$

$$v_{zjk+\frac{1}{2}}^b = w_{jk+\frac{1}{2}}^l v_{zj-\frac{1}{2}k} + w_{jk+\frac{1}{2}}^r v_{zj+\frac{1}{2}k}, \quad (27b)$$

where the left and right weights, summing to unity, are defined as

$$w_{jk+\frac{1}{2}}^l = \frac{m_{j-\frac{1}{2}k+\frac{1}{2}}}{m_{j-\frac{1}{2}k+\frac{1}{2}} + m_{j+\frac{1}{2}k+\frac{1}{2}}}, \quad (28a)$$

$$w_{jk+\frac{1}{2}}^r = \frac{m_{j+\frac{1}{2}k+\frac{1}{2}}}{m_{j-\frac{1}{2}k+\frac{1}{2}} + m_{j+\frac{1}{2}k+\frac{1}{2}}}. \quad (28b)$$

Similar to Eq. (13), at the liner's inner and outer surfaces, these weights are reduced to

$$w_{0k-\frac{1}{2}}^l = w_{N_r k-\frac{1}{2}}^r = 0, \quad w_{0k-\frac{1}{2}}^r = w_{N_r k-\frac{1}{2}}^l = 1, \quad k = 1, \dots, N_z.$$

The remaining fluxes become

$$q_{jk}^{M_r} = \frac{q_{jk}^m}{2} (v_{rjk-\frac{1}{2}} + v_{rjk+\frac{1}{2}}), \quad (29a)$$

$$q_{j+\frac{1}{2}k+\frac{1}{2}}^{M_z} = \frac{q_{j+\frac{1}{2}k+\frac{1}{2}}^m}{2} (v_{zj+\frac{1}{2}k} + v_{zj+\frac{1}{2}k+1}), \quad (29b)$$

$$q_{jk}^L = \frac{(m_{jk-\frac{1}{2}} v_{zjk-\frac{1}{2}}^t r_{jk+\frac{1}{2}}^2 + m_{jk+\frac{1}{2}} v_{zjk+\frac{1}{2}}^b r_{jk-\frac{1}{2}}^2) (w_{jk-\frac{1}{2}} + w_{jk+\frac{1}{2}})}{4\Delta z}, \quad (29c)$$

where the corresponding mass fluxes are given by expressions consistent with the control volume masses definition (12),

$$q_{jk}^m = \frac{1}{2} (q_{j-\frac{1}{2}k}^m + q_{j+\frac{1}{2}k}^m), \quad (30a)$$

$$q_{j+\frac{1}{2}k+\frac{1}{2}}^m = \frac{1}{2} (q_{j+\frac{1}{2}k}^m + q_{j+\frac{1}{2}k+1}^m). \quad (30b)$$

The axial pressure force shear term is

$$\begin{aligned} \delta f_{zj+\frac{1}{2}k}^p &= w_{jk-\frac{1}{2}}^r \Delta p_{jk-\frac{1}{2}} \pi (r_{jk}^2 - r_{jk-\frac{1}{2}}^2) + w_{jk+\frac{1}{2}}^r \Delta p_{jk+\frac{1}{2}} \pi (r_{jk+\frac{1}{2}}^2 - r_{jk}^2) \\ &+ w_{j+1k-\frac{1}{2}}^l \Delta p_{j+1k-\frac{1}{2}} \pi (r_{j+1k}^2 - r_{j+1k-\frac{1}{2}}^2) \\ &+ w_{j+1k+\frac{1}{2}}^l \Delta p_{j+1k+\frac{1}{2}} \pi (r_{j+1k+\frac{1}{2}}^2 - r_{j+1k}^2), \end{aligned} \quad (31)$$

where the radial pressure difference is introduced as

$$\Delta p_{jk+\frac{1}{2}} = p_{j+\frac{1}{2}k+\frac{1}{2}} - p_{j-\frac{1}{2}k+\frac{1}{2}}.$$

Let us make several comments about energy balance in the ISM-hydro scheme. The discrete form of the liner kinetic energy balance follows from Eq. (B5) [cf. Eq. (25)]:

$$\dot{E}_{kin} = \sum_{j,k} p_{j+\frac{1}{2}k+\frac{1}{2}} (\nabla \cdot \mathbf{v})_{j+\frac{1}{2}k+\frac{1}{2}} V_{j+\frac{1}{2}k+\frac{1}{2}} + W, \quad (32)$$

where  $W$  denotes the overall power of the external pressure forces from gases in the channel inlets and inside the cavity [see Eq. (34)]. This equation can be used as an extra diagnostic of the correctness of the solution: for all times  $t$ , the discrete kinetic energy of the liner (B4) must be equal to the time integral of Eq. (32) within the time integration error. In addition, we can introduce a discrete equation for the dynamics of the fluid internal energy in every mesh cell (assuming no thermal diffusion for simplicity)

$$\dot{U}_{j+\frac{1}{2}k+\frac{1}{2}} = q_{j+\frac{1}{2}k}^U - q_{j+\frac{1}{2}k+1}^U - p_{j+\frac{1}{2}k+\frac{1}{2}} (\nabla \cdot \mathbf{v})_{j+\frac{1}{2}k+\frac{1}{2}} V_{j+\frac{1}{2}k+\frac{1}{2}}, \quad (33)$$

where  $q_{j+\frac{1}{2}k}^U$  and  $q_{j+\frac{1}{2}k+1}^U$  are the advective fluxes of internal energy through the bottom and top boundaries of the cell, respectively. Of course, to properly include internal energy in the numerical scheme, we would also need to define it in terms of thermodynamic variables (density and temperature) according to the chosen equation of state (20). This is not part of our analysis; here, we simply want to demonstrate that the ISM-hydro scheme is compatible with a discrete form of energy conservation. Summing up Eqs. (32) and (33) over all fluid cells, we obtain the energy conservation law in its discrete form

$$\frac{d}{dt} \left( E_{kin} + \sum_{j,k} U_{j+\frac{1}{2}k+\frac{1}{2}} \right) = W,$$

i.e., the change in the total fluid energy is equal to the work done by external pressure forces. The presence of the discrete energy conservation law puts more constraints on the numerical scheme and, thus, helps to avoid spurious solutions.

System (5) should be supplemented with boundary conditions. Due to the staggering of the velocity components, we only require impenetrable boundary conditions at the end plates for the axial velocity

$$v_{zj-\frac{1}{2}} = v_{zj-\frac{1}{2}N_z} = 0, \quad j = 1, \dots, N_r.$$

This means we do not need to solve the axial momentum equation (5c) for corresponding control volumes and all fluxes through the end plates are zero. For determining pressure forces in Eqs. (5b) and (5c), in addition to pressures inside the fluid cells given by Eq. (21), we define pressures just outside the liner's inner and outer surfaces as corresponding gas pressures, namely,

$$P_{-\frac{1}{2}k-\frac{1}{2}} = P_0 \left( \frac{V_{in}(0)}{V_{in}(t)} \right)^\gamma, \quad V_{in}(t) = \sum_{k=1}^{N_z} \Delta z \pi r_{0k-\frac{1}{2}}^2(t), \quad (34a)$$

$$P_{N_r+\frac{1}{2}k-\frac{1}{2}} = P_{i(k)}(t), \quad i(k) = \left\lceil \frac{k}{K_c} \right\rceil, \quad k = 1, \dots, N_z, \quad (34b)$$

where the first equation is the pressure of the ideal gas adiabatically compressed inside the cavity with changing volume  $V_{in}(t)$ , and  $P_{i(k)}(t)$  is the driving gas pressure pushing on the outer surface of the  $k$ th horizontal fluid layer in the  $i$ th channel, with the formal relation between indices  $i$  and  $k$  given by the ceiling function.

Additional conditions are imposed on discrete quantities inside the rotor channels (regions between baffles). First, all the vertical cell sizes  $\Delta z$  are shrunk by a factor  $1 - b$ , where  $b$  is the obstruction

fraction due to the thickness of the baffles. That is, the vertical area becomes

$$S_{jk+\frac{1}{2}} = 2\pi r_{jk+\frac{1}{2}} \Delta z (1 - b) \text{ if } R_a \leq r_{jk+\frac{1}{2}}, \quad (35)$$

and the volume of a cell, located fully or partially inside a channel, becomes

$$V_{jk+\frac{1}{2}} = \begin{cases} \pi \Delta z (1 - b) (r_{j+1k+\frac{1}{2}}^2 - r_{jk+\frac{1}{2}}^2) & \text{if } R_a \leq r_{jk+\frac{1}{2}} < r_{j+1k+\frac{1}{2}}, \\ \pi \Delta z ((1 - b) (r_{j+1k+\frac{1}{2}}^2 - R_a^2) + R_a^2 - r_{jk+\frac{1}{2}}^2) & \text{if } r_{jk+\frac{1}{2}} < R_a < r_{j+1k+\frac{1}{2}}. \end{cases} \quad (36)$$

Second, the axial velocity and all corresponding fluxes are set to zero for a control volume  $(j + 1/2, k)$  if half or more of its horizontal area overlaps with the  $i$ th baffle

$$v_{j+\frac{1}{2}k} = 0 \quad \text{if } R_a^2 \leq \frac{1}{2} (r_{jk}^2 + r_{j+1k}^2) \quad \text{and} \quad k = iK_c.$$

If we consider one horizontal mesh layer per channel ( $N_z = N_c$ ), then, inside every channel, system (5) simplifies to

$$m_{jk+\frac{1}{2}} = \text{constant}, \quad (37a)$$

$$\omega_{jk+\frac{1}{2}} r_{jk+\frac{1}{2}}^2 = \text{constant}, \quad (37b)$$

$$m_{jk+\frac{1}{2}} \ddot{r}_{jk+\frac{1}{2}} = m_{jk+\frac{1}{2}} \omega_{jk+\frac{1}{2}}^2 r_{jk+\frac{1}{2}} - S_{jk+\frac{1}{2}} (p_{j+\frac{1}{2}k+\frac{1}{2}} - p_{j-\frac{1}{2}k+\frac{1}{2}}), \quad (37c)$$

which are the trivial equations of motion of particles with constant masses and angular momenta. In [Appendix C](#), we show that these equations can be derived from the Lagrangian formalism.

### C. Initial conditions and time stepping

We now outline the initialization and time integration procedures used in ISM-hydro. [Table I](#) summarizes the input parameters of the problem.

At time  $t = 0$ , the liner rotates at angular velocity  $\omega = \Omega_0$ . The radial distribution of fluid pressure balances the centrifugal forces

$$m_{jk-\frac{1}{2}} \Omega_0^2 r_{jk-\frac{1}{2}} = S_{jk-\frac{1}{2}} (p_{j+\frac{1}{2}k-\frac{1}{2}} - p_{j-\frac{1}{2}k-\frac{1}{2}}), \quad j = 0, \dots, N_r, \quad (38)$$

where the masses of the control volumes and pressures in the fluid cells are given by

$$m_{jk-\frac{1}{2}} = \frac{1}{2} (m_{j-\frac{1}{2}k-\frac{1}{2}} + m_{j+\frac{1}{2}k-\frac{1}{2}}), \quad j = 0, \dots, N_r, \quad (39a)$$

$$m_{j-\frac{1}{2}k-\frac{1}{2}} = m_{N_r+\frac{1}{2}k-\frac{1}{2}} = 0, \quad m_{j-\frac{1}{2}k-\frac{1}{2}} = \rho_{j-\frac{1}{2}k-\frac{1}{2}} V_{j-\frac{1}{2}k-\frac{1}{2}}, \quad j = 1, \dots, N_r, \quad (39b)$$

$$p_{j-\frac{1}{2}k-\frac{1}{2}} = p_0, \quad p_{j-\frac{1}{2}k-\frac{1}{2}} = \frac{\rho_0 c_s^2}{\Gamma} \left( \left( \frac{\rho_{j-\frac{1}{2}k-\frac{1}{2}}}{\rho_0} \right)^\Gamma - 1 \right), \quad j = 1, \dots, N_r, \quad (39c)$$

and the vertical areas and volumes of the fluid cells are determined using Eqs. (17a) and (11) or Eqs. (35) and (36) based on the initial vertical mesh lines  $r_j|_{t=0}$ . The index  $k$  in the above equations spans the range  $k = 1, \dots, N_z$ . Since the initial shape of the liner is cylindrical

**TABLE I.** List of model input parameters.

Parameter	Value	Description
Geometry of the rotor		
$H$ (m)	5	Height of rotor
$R_a$ (m)	2.2	Inner radius of channels (baffles)
$R_b$ (m)	3.5	Outer radius of channels (baffles) and rotor
$N_c$	50	Number of channels (inlets)
$b$	0.2	Baffles obstruction fraction
Properties of the liner (liquid lithium)		
$\rho_0$ (kg/m <sup>3</sup> )	500	Reference density in EOS
$c_s$ (m/s)	4500	Speed of sound in EOS
$\Gamma$	6	Stiffness exponent in EOS
$R_0$ (m)	2	Initial inner radius
$\Omega_0$ (rad/s)	50	Initial angular velocity
Properties of the ideal gas in the cavity		
$\gamma$	1.4	Adiabatic index
$p_0$ (Pa)	$10^4$	Initial pressure

and no quantities are dependent on  $z$ , these equations are identical for every horizontal layer.

For the initialization step, we solve Eq. (38) with substitutions from Eq. (39) using a fixed-point iterative method for unknown cell densities  $\rho_{j-1/2k-1/2}$ . Every iteration proceeds as follows: the current cell densities are used to calculate cell masses with Eqs. (39a) and (39b), then the pressure distribution is determined from Eq. (38), and the cell densities are updated based on the corresponding cell pressures using Eq. (39c). Iterations start with  $\rho_{j-1/2k-1/2} = \rho_0$  and run until the change in cell densities between two consecutive iterations is below a specified tolerance. Equation (38) contains  $N_r + 1$  scalar equations for every value of  $k - 1/2$ ; this allows us to determine densities (and, consequently, masses and pressures) in all  $N_r$  mesh cells of a horizontal layer plus the pressure value  $p_{N_r+1/2k-1/2}$ , which corresponds to the total centrifugal pressure exerted by the rotating liner at  $r = R_b$ ,

$$p_{cf} = p_{N_r+1/2k-1/2}. \quad (40)$$

In order to push the liner inward, the driving pressure must exceed  $p_{cf}$ .

We implement an explicit Runge-Kutta second order method (RK2, also known as the midpoint method) for integration of system (5) in time. The simulation time step  $\Delta t$  is a case specific constant chosen to ensure numerical stability;  $N_t$  is the number of time steps. The ISM-hydro algorithm is outlined in [Algorithm 1](#), where matrices (denoted by bold symbols with a hat) correspond to two-dimensional arrays of mesh-discretized quantities (e.g.,  $\hat{\mathbf{r}} = \{r_{jk+\frac{1}{2}}\}$ ,  $\hat{\mathbf{m}} = \{m_{j+1/2k+\frac{1}{2}}\}$ ,  $\hat{\mathbf{v}}_z = \{v_{zj+\frac{1}{2}k}\}$ ). We also define matrices for the mass related to vertical and horizontal cell faces,  $\hat{\mathbf{m}}_{ver} = \{m_{jk+\frac{1}{2}}\}$  and  $\hat{\mathbf{m}}_{hor} = \{m_{j+1/2k}\}$ , and introduce the state vector  $\mathbf{s}$  for compact notation

$$\mathbf{s} = (t, \hat{\mathbf{r}}, \hat{\mathbf{m}}, \hat{\mathbf{M}}_F, \hat{\mathbf{M}}_z, \hat{\mathbf{L}}).$$

In ISM-hydro, this algorithm is implemented using the MATLAB programming language.<sup>14</sup>

**ALGORITHM 1** ISM-hydro algorithm with Runge–Kutta second order method (RK2).

---

**Input:** parameters from Table I,  $N_r$ ,  $N_z$ ,  $\Delta t$ ,  $N_p$ , and  $\nu$   
 Set RK2 coefficients  $c_1 = 1/2$  and  $c_2 = 1$   
 Set initial mesh  $\hat{\mathbf{r}}$ ,  $\hat{\mathbf{z}}$ , find cell volumes and areas  
 Find initial cell masses  $\hat{\mathbf{m}}$  and centrifugal liner pressure  $p_{cf}$   
**Input:** driving pressures  $P_i(t)$   
 Set initial state vector  $\mathbf{s} = (0, \hat{\mathbf{r}}, \hat{\mathbf{m}}, \hat{\mathbf{0}}, \hat{\mathbf{0}}, \hat{\mathbf{m}}_{ver} \hat{\mathbf{r}}^2 \Omega_0)$   
**for**  $n = 1$  to  $N_t$  **do** \*\* Time stepping loop  
 $\mathbf{s}_0 = \mathbf{s}$   
**for**  $l = 1$  to 2 **do** \*\* Stages of RK2  
 Find cell volumes and areas for current mesh  $\hat{\mathbf{r}}$ ,  $\hat{\mathbf{z}}$   
 Find cell densities  $\hat{\rho}$  and pressures  $\hat{p}$   
 Find pressure in cavity and driving pressures  
 Find control volume masses  $\hat{\mathbf{m}}_{ver}$  and  $\hat{\mathbf{m}}_{hor}$  from cell masses  $\hat{\mathbf{m}}$   
 Find  $\hat{\mathbf{v}}_r$ ,  $\hat{\mathbf{v}}_z$ ,  $\hat{\mathbf{r}}$  and  $\hat{\omega}$  from state vector  $\mathbf{s}$   
 Set elements of  $\hat{\mathbf{v}}_z$  inside channels to 0, adjust  $\hat{\mathbf{v}}_r$ ,  $\hat{\mathbf{M}}_r$  and  $\hat{\mathbf{M}}_z$   
**if**  $l = 1$  **then** \*\* Save quantities only at full time step  
 Save quantities  $t$ ,  $\hat{\mathbf{r}}$ ,  $\hat{\mathbf{m}}$ ,  $\hat{\mathbf{v}}_z$ ,  $\hat{\omega}$ ,  $\hat{p}$   
**end if**  
 Find RHS of system (5), i.e., time derivatives  $\hat{\mathbf{m}}$ ,  $\hat{\mathbf{M}}_r$ ,  $\hat{\mathbf{M}}_z$ ,  $\hat{\mathbf{L}}$   
 Set time derivative of state vector  $\hat{\mathbf{s}} = (1, \hat{\mathbf{r}}, \hat{\mathbf{m}}, \hat{\mathbf{M}}_r, \hat{\mathbf{M}}_z, \hat{\mathbf{L}})$   
 Do RK2 stage  $\mathbf{s} = \mathbf{s}_0 + c_l \Delta t \hat{\mathbf{s}}$   
**end for**  
**end for**  
**Output:** saved quantities

---

### III. CONVERGENCE STUDY AND COMPARISON WITH OPENFOAM

#### A. OpenFOAM solver and setup

OpenFOAM 10 is an open-source C++ toolbox used for the customization and extension of numerical solvers for continuum mechanics problems, especially suited for computational fluid dynamics (CFD). Its multiphase solvers have been validated against experimental data relevant to GF's MTF concept.<sup>3</sup> They have also been successfully verified and extended to account for magnetohydrodynamic effects in an axisymmetric geometry.<sup>2</sup> In the present study, we work with compressibleInterFoam—an OpenFOAM solver for two compressible, non-isothermal, and immiscible fluids with interface capturing based on the volume of fluid (VOF) approach.<sup>15</sup> Foundational papers on the current solver implementation include Refs. 16–18.

Under the VOF framework, an indicator function  $\alpha$ , also called volume phase fraction, is defined as the fractional volume of the cell occupied by a certain fluid. By convention in Sec. III, its value can vary continuously from  $\alpha = 1$  for a cell full of liquid to  $\alpha = 0$  for a cell full of gas, and the  $\alpha = 0.5$  isocontour is extracted whenever the free surface location is reported,

$$\alpha = \frac{V_{\text{liquid}}}{V_{\text{cell}}} = \begin{cases} 1 & \text{if liquid,} \\ 0.5 & \text{if free surface,} \\ 0 & \text{if gas.} \end{cases}$$

All the fluid properties entering the Navier–Stokes equations are then defined as an  $\alpha$ -weighted average between two phases; for example, the density is

$$\rho = \alpha \rho_{\text{liquid}} + (1 - \alpha) \rho_{\text{gas}}.$$

The OpenFOAM governing equations include the mass conservation, momentum, and energy equations, as well as an additional transport equation for the  $\alpha$  field. They are solved using the PIMPLE algorithm.<sup>19</sup> In the liquid phase, we consider equation of state (20) and zero shear viscosity so that the governing equations become equivalent to system (1). In the gas phase, we solve the ideal gas law to approximate ISM-hydro's pressure boundary condition (34a). Similar to Sec. II, gravity, surface tension, and shear viscosity are not considered.

Slip boundary conditions are used for all walls (end plates and baffles). Driving pressures are prescribed for all channel inlets at  $r = R_b$ , uniformly across each inlet. Gas phase ( $\alpha = 0$ ) is injected at all inlets, with a high temperature of  $10^4$  K. The temperature is also initialized to  $10^4$  K in the full domain. High temperatures ensure rapid pressure equilibration in each gas region (cavity and each channel) in order to approximate ISM-hydro's pressure boundary conditions (34a) and (34b). The velocity and pressure fields are initialized in the liner region to match ISM-hydro fields after the initialization step of Sec. II C.

Taking advantage of the symmetries of the test cases introduced in Sec. III B below, the OpenFOAM computational domain is reduced to either half of a horizontal layer for the cylindrical case (i) (with a symmetry plane located at the midplane of the layer), or half of the rotor geometry for the shaped cases (ii) and (iii) (with a symmetry plane located at the equatorial plane  $z = 0$ ). Since the problem is axisymmetric, the three-dimensional OpenFOAM mesh is a wedge-shaped slice with only one cell across the azimuthal direction and a wedge angle of  $3^\circ$ . The mesh is structured with uniform square cells in the  $r$ - $z$  plane (cell sizes  $\Delta r = \Delta z$ ). For all cases, an adaptive time-stepping scheme is selected, with a maximum time step of  $\Delta t_{\text{max}} = 5 \times 10^{-8}$  s. No turbulence modeling is applied.

#### B. Test cases description

Here, we describe the setup of three test cases, two of which (the main test cases) are used for a convergence study and a detailed comparison between ISM-hydro and OpenFOAM, while the third one is used to demonstrate the limitations of the ISM-hydro method. We consider the rotor geometry described in Sec. II A with specific values of the parameters relevant to GF's MTF concept listed in Table I. In particular, we assume that the liner material is liquid lithium.

The initial simulation setup and the resulting liner implosions for the main test cases are illustrated in Fig. 3, using results from OpenFOAM. Figure 3(a) displays a cross-sectional ( $r$ - $z$  plane) view of the full OpenFOAM geometry at time  $t = 0$ , colored by the  $\alpha$  field. All investigated test cases differ only in their applied driving pressures, as described below.

- (i) A cylindrical implosion test case [cylindrical case, Fig. 3(b)]. This case assumes the same driving gas pressure for all inlets. The liner's inner surface remains cylindrical throughout the implosion. As the liner is driven inward, the gas inside the cavity becomes pressurized (by adiabatic compression) and the liner centrifugal force increases (by angular momentum conservation) until the liner's inner surface radial velocity changes sign at the turnaround point.
- (ii) A shaped implosion test case [shaped case, Fig. 3(c)]. This case assumes a larger driving gas pressure near the end plates compared to the equatorial plane. More liquid is being pushed out

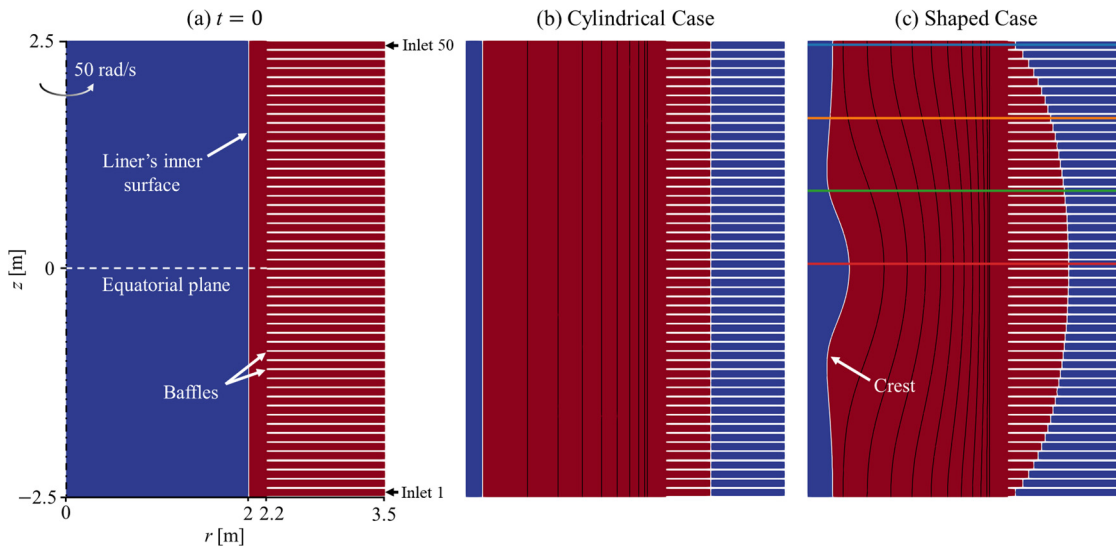


**FIG. 3.** The main test cases illustrated with OpenFOAM results. All panels display a cross-sectional ( $r$ - $z$  plane) view of the rotor geometry colored by the  $\alpha$  field (with liner in red and ideal gas in blue). (a) Time  $t = 0$  for all cases. (b) Cylindrical case at time  $t = 10$  ms, 0.2 ms before turnaround. (c) Shaped case at time  $t = 12$  ms, 0.4 ms before peak implosion. The colored horizontal lines correspond to the four elevations highlighted in Figs. 4 (driving pressures) and 8 (implosion trajectory), with matching colors. In panels (b) and (c), the black lines inside the liner indicate the liner's inner surface at 1 ms intervals (time  $t = 0$  excluded).

of the channels near the end plates. As a result, the inner surface gradually deviates from cylindricity and forms two waves. Their crests propagate toward the equatorial plane. Turnaround happens near the end plates first, and at a larger radius, compared to the equatorial plane. Peak implosion refers to the point in time when turnaround occurs at the equatorial plane.

- (iii) A strongly shaped implosion test case with breaking surface waves (strongly shaped case, not shown in Fig. 3). This case is analogous to the shaped case, but assumes increased magnitudes of driving gas pressures. The resulting two surface waves break near peak implosion (their crests overturn). This test case exemplifies the limitations of the ISM-hydro method.

We assume that for each channel inlet  $i$ , the driving gas pressure  $P_i(t)$  is a linear ramp followed by a plateau, which is an approximation of pressures generated by the pneumatic driving system

$$P_i(t) = \begin{cases} p_{cf} + (P_i^{\max} - p_{cf}) \frac{t}{\tau} & \text{if } t < \tau, \\ P_i^{\max} & \text{otherwise,} \end{cases} \quad (41)$$

where  $p_{cf}$  is the total centrifugal pressure from the ISM-hydro initialization step [defined in Eq. (40)],  $P_i^{\max}$  is a pressure plateau value, and  $\tau$  is a pressure ramp time constant chosen to be  $\tau = 1$  ms for all test cases. For the cylindrical case,  $P_i^{\max}$  is the same for all inlets  $i$ . A parabolic parametrization, symmetric with respect to the equatorial plane, is used to define  $P_i^{\max}$  as a function of inlet  $i$  in a more general setting

$$P_i^{\max} = P^{\max} \left( 1 + \varepsilon \left( \left( \frac{2(i-0.5)}{N_c} - 1 \right)^2 - 1 \right) \right), \quad i = 1, \dots, N_c, \quad (42)$$

where  $P^{\max}$  is the pressure plateau value at the end plates, and the dimensionless parameter  $\varepsilon$  characterizes the vertical variation of driving pressures ( $\varepsilon = 0$  means no variation). We consider

- (i)  $P^{\max} = 27$  MPa,  $\varepsilon = 0$  for the cylindrical case;
- (ii)  $P^{\max} = 27$  MPa,  $\varepsilon = 0.35$  for the shaped case;
- (iii)  $P^{\max} = 40.5$  MPa,  $\varepsilon = 0.35$  for the strongly shaped case.

The driving gas pressures for the main test cases (i) and (ii) are displayed in Fig. 4.

Driving pressures and parameters listed in Table I are chosen such that the implosion time scales and turnaround radii are relevant to GP's MTF concept. For example, in the cylindrical case, turnaround occurs when the liner's inner radius becomes approximately 20 times smaller than its initial value  $R_0 = 2$  m. Also, the liner's inner surface is Rayleigh-Taylor stable at all times for all test cases. The ideal gas inside the cavity does not affect the implosion dynamics; its pressure is negligible compared to liner centrifugal forces and driving pressures.

### C. ISM-hydro spatial convergence study

In this section, we investigate the spatial (mesh) convergence of ISM-hydro for main test cases (i) and (ii) and demonstrate that ISM-hydro implosion trajectories closely approach those from OpenFOAM as resolution in both codes is increased. To facilitate the convergence study, we introduce radially non-uniform initial meshes with notation

$$N_r = {}^{N_1} N_0,$$

which are constructed from a usual uniform mesh with  $N_0$  radial cells by further dividing the innermost cell into  $N_1$  equal sub-cells (for a total of  $N_0 + N_1 - 1$  cells in the radial direction). Since the liner rebounds due to centrifugal forces in these test cases, ISM-hydro's solution accuracy is strongly dependent on the local mesh resolution

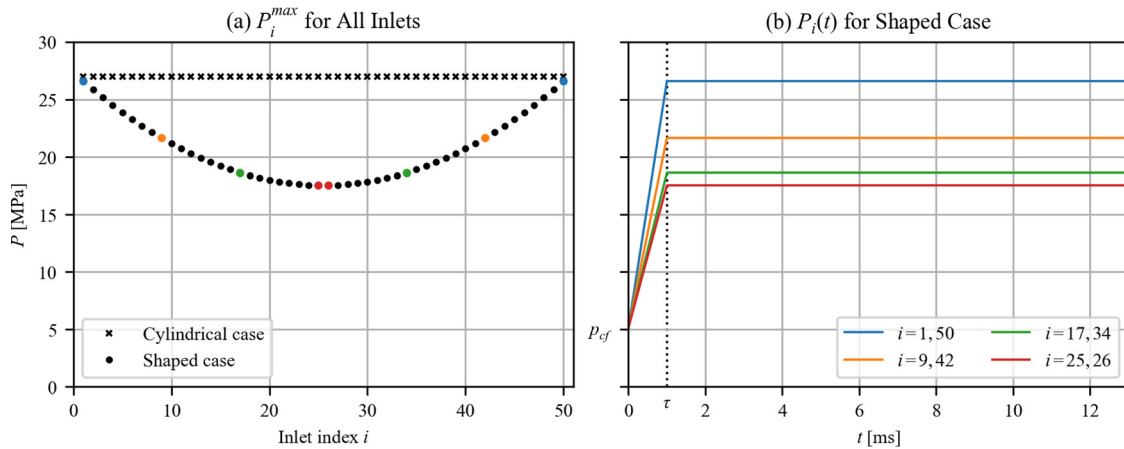


**FIG. 4.** Driving pressure boundary conditions: (a) driving gas pressure plateau value as a function of inlet  $i$  for the main test cases and (b) driving gas pressure as a function of time for the inlets highlighted in panel (a) with matching colors (shaped case). The vertical dotted line indicates  $t = \tau$ , the pressure ramp time constant.

near the liner's inner surface (large centrifugal forces are concentrated in this region near peak implosion). Non-uniform initial meshes with finer resolution near the liner's inner surface can speed up simulations while preserving high accuracy.

Figure 5 displays the results of a convergence study for the cylindrical case. In ISM-hydro, this case is equivalent to a one-dimensional simulation with  $N_z = N_c = 1$ . Figure 5(a) shows the full implosion trajectory predicted by the two codes (highest resolution only), while other panels zoom in on turnaround to visualize convergence of each code. Figure 5(b) demonstrates that the implosion trajectory converges as the number of radial cells  $N_r$  is increased. It also confirms that solution accuracy strongly depends on the local resolution near the liner's inner surface, since  $N_r = 400$  and  $N_r = 850$  yield very similar trajectories. Figure 5(c) shows that the OpenFOAM implosion trajectory also converges as the cell size  $\Delta r$  is decreased. OpenFOAM predicts a slightly slower and deeper implosion compared to ISM-hydro. This

small discrepancy is due to differing gas treatments. The gas dynamics in OpenFOAM are two-dimensional with small pressure waves and nonuniformities in the cavity and the rotor channels, while the gas pressures in ISM-hydro follow zero-dimensional equations (34a) and (34b).

Figure 6 displays the results of a convergence study for the shaped case. Here, we consider only the equatorial implosion trajectory (at  $z = 0$ ) and report the data near peak implosion. Figure 6(a) shows the ISM-hydro trajectory convergence as we increase  $N_z$ , while keeping the same radially non-uniform mesh with  $N_r = 10^{10} 20$ . Note that when changing  $N_z$ , we also change the number of rotor channels  $N_c$  such that  $N_c = N_z$ . The driving gas pressures at the channel inlets are still given by Eqs. (41) and (42) with corresponding  $N_c$ . Similarly, Fig. 6(b) shows trajectory convergence as  $N_r$  is increased for a fixed  $N_z = N_c = 50$ . We observe that simulations with  $N_r = 850$  and  $N_r = 400$  yield very similar results again, but the run time for the

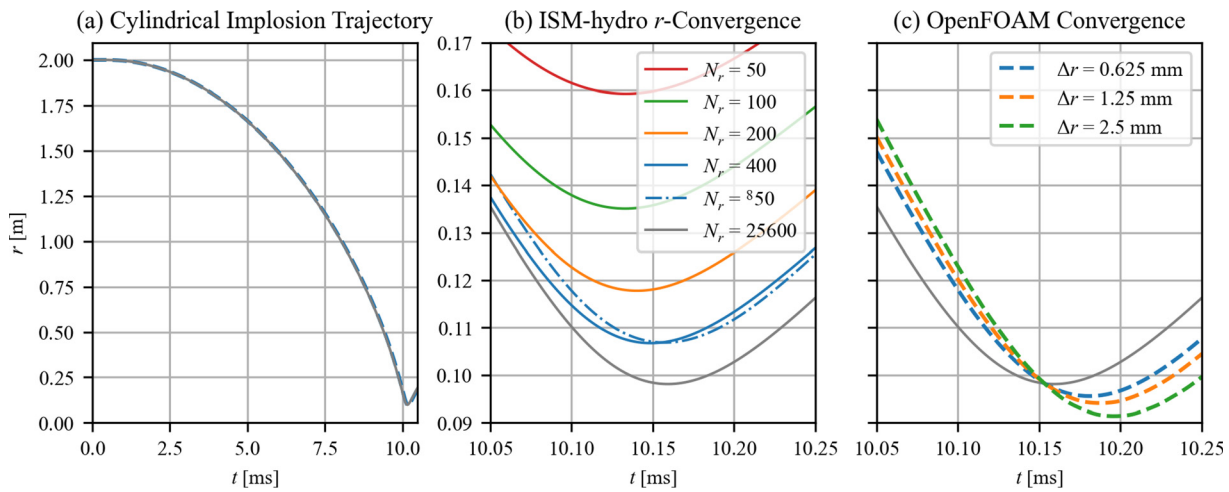


**FIG. 5.** Cylindrical case convergence study: (a) full implosion trajectory (highest resolution only), (b) ISM-hydro convergence as  $N_r$  is increased ( $N_z = N_c = 1$ ), and (c) OpenFOAM convergence. Panels (b) and (c) are zoomed-in views centered near turnaround.

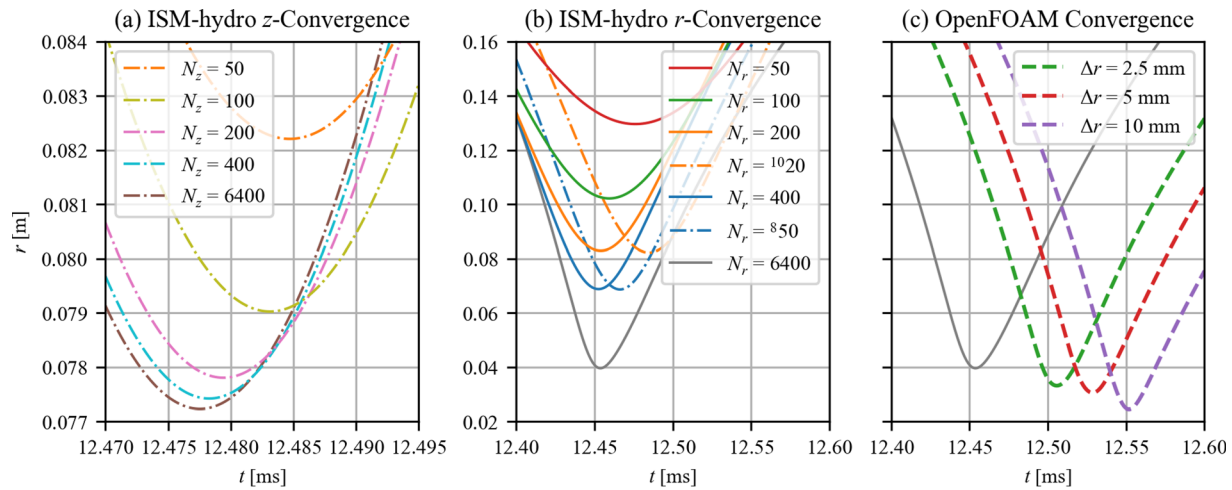


**FIG. 6.** Shaped case convergence study (equatorial implosion trajectory): (a) ISM-hydro convergence as  $N_z$  is increased at fixed  $N_r = 10^{20}$ , (b) ISM-hydro convergence as  $N_r$  is increased at fixed  $N_z = 50$ , and (c) OpenFOAM convergence. All panels are zoomed-in views centered near peak implosion.

former ( $\sim 80$  s) is almost seven times shorter; see Table II. This confirms that ISM-hydro can be both fast and accurate if radially non-uniform meshes are used. Figure 6(c) displays the same trend as Fig. 5(c): OpenFOAM results converge, and a similar discrepancy in time and depth is observed between the two codes. Table II summarizes the ISM-hydro simulations used in the shaped case convergence study.

To estimate the order of spatial convergence (order of accuracy) of ISM-hydro, we define the average truncation error between two consecutive approximations of the liner's implosion trajectory (inner surface radius) as

**TABLE II.** ISM-hydro shaped case simulations used in the spatial (mesh) convergence study. Results from the simulation with  $N_r = 6400$  are used for comparison with OpenFOAM in Sec. III D.

$N_r$	$N_z$	$\Delta t$ ( $\mu$ s)	$\nu$ ( $\text{m}^2/\text{s}$ )	Run time (s)
50	50	2	64	8.55
100	50	1	32	33.3
200	50	0.5	16	136
400	50	0.25	8	539
850	50	0.25	8	78.2
800	50	0.125	4	2213
1600	50	0.0625	2	10010
3200	50	0.03125	1	42566
6400	50	0.015625	0.5	200403
10 <sup>20</sup>	50	0.5	25	29.1
10 <sup>20</sup>	100	0.5	25	48.7
10 <sup>20</sup>	200	0.5	25	93.9
10 <sup>20</sup>	400	0.5	25	162
10 <sup>20</sup>	800	0.5	25	288
10 <sup>20</sup>	1600	0.125	25	2137
10 <sup>20</sup>	3200	0.03125	25	15610
10 <sup>20</sup>	6400	0.0078125	25	151911

$$e_N = \langle |r_0(t, z; N) - r_0(t, z; 2N)| \rangle_{t, z},$$

where angle brackets with subscripts denote averaging over the total implosion time and height of the liner, and  $N$  refers to the mesh resolution in either the radial ( $N = N_r$ ) or axial ( $N = N_z$ ) direction. In Fig. 7, we report the average truncation errors  $e_N$  for the trajectories of Figs. 5 and 6 with a total implosion time of 13 ms. From their asymptotic behaviors, we can infer the corresponding orders of mesh convergence in ISM-hydro

$$e_N = \begin{cases} \mathcal{O}(N_r^{-1}) & \text{for the cylindrical case,} \\ \mathcal{O}(N_r^{-1}) & \text{for the shaped case, } N_z \text{ fixed,} \\ \mathcal{O}(N_z^{-1}) & \text{for the shaped case, } N_r \text{ fixed.} \end{cases}$$

Therefore, the ISM-hydro method has overall first order accuracy in space, as expected from the analysis in Sec. II B.

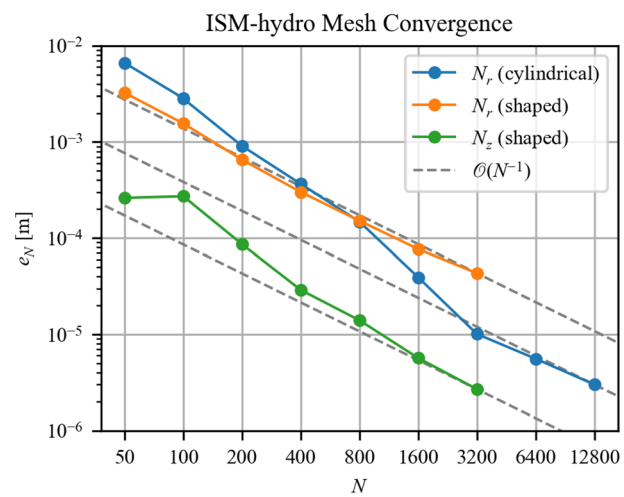


**FIG. 7.** ISM-hydro average truncation error  $e_N$  for different resolutions and test cases.

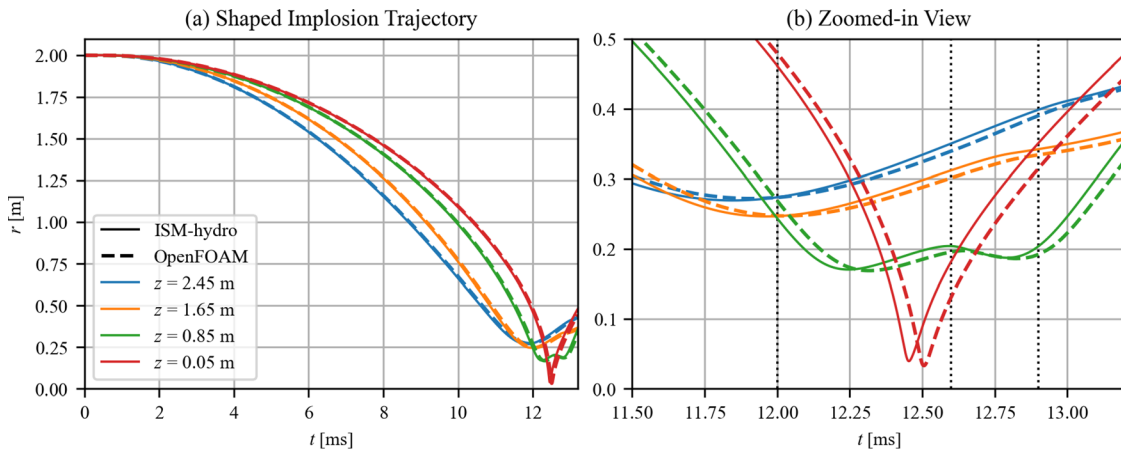


**FIG. 8.** Shaped case implosion trajectory. The liner's inner surface trajectory is plotted against time at four different elevations shown with corresponding colors in Fig. 3(c). (a) Full implosion trajectory. (b) A zoomed-in view centered near peak implosion. The vertical dotted lines indicate  $t = 12$ ,  $t = 12.6$ , and  $t = 12.9$  ms, corresponding to the highlighted times of Figs. 9–13.

#### D. Comparison with OpenFOAM

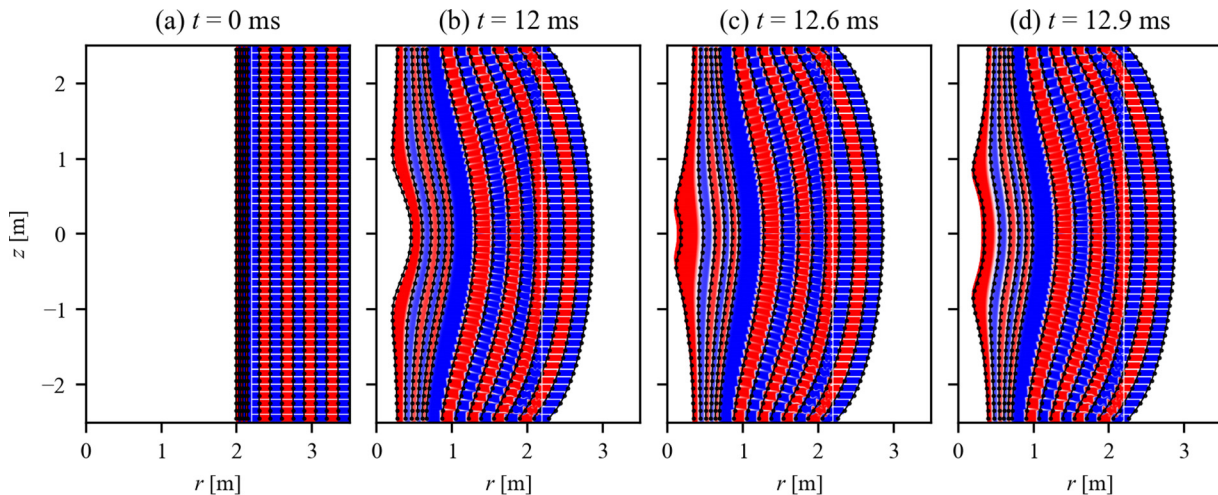
After establishing the spatial convergence of ISM-hydro, in this section, we demonstrate that ISM-hydro converges to a solution that is very close to the one obtained with OpenFOAM. For this purpose, we show in Figs. 8–13 quantitative and qualitative comparisons between the highest resolution ISM-hydro and OpenFOAM simulations of the shaped case. The OpenFOAM test case and simulation results are provided.<sup>20</sup>

Figure 8 displays the liner's inner surface trajectory at four different elevations. The trend is similar to results in Figs. 5 and 6; ISM-hydro predicts a slightly faster implosion. Note that a similar time discrepancy can be observed at all elevations, suggesting that the predicted shapes are comparable for both codes but shifted in time. The magnitude of this time shift is also consistent with the cylindrical case results in Fig. 5.

In Figs. 9–13, four specific times are highlighted throughout the implosion. In chronological order: (a)  $t = 0$  ms, initial simulation time; (b)  $t = 12$  ms, roughly 0.5 ms before peak implosion; (c)  $t = 12.6$  ms, roughly 0.1 ms after peak implosion; (d)  $t = 12.9$  ms, roughly 0.4 ms after peak implosion. The gas phase is masked out in all results.

In Figs. 9–12, liner fields in the  $r$ - $z$  plane are visualized and compared for the two codes. The four panels correspond to the four times listed above, in chronological order from the left to the right. All the information contained in Figs. 9–12 is condensed into a single animation<sup>20</sup> from  $t = 0$  to  $t = 13.2$  ms with a minimum time sampling of  $10\ \mu\text{s}$  around peak implosion.

Figure 9 is particularly informative as it reveals internal flow patterns. An OpenFOAM passive scalar is introduced at time  $t = 0$  marking a specific partition of the liner into vertical layers, which corresponds to a radially non-uniform initial mesh with  $N_r = 510$ .



**FIG. 9.** Vertical fluid layer deformations at four highlighted times. A subset of ISM-hydro vertical mesh lines (black dotted lines) is superimposed on the OpenFOAM passive scalar field (alternating red and blue layers). These mesh lines and passive scalar field are advected with the fluid flow in corresponding codes.

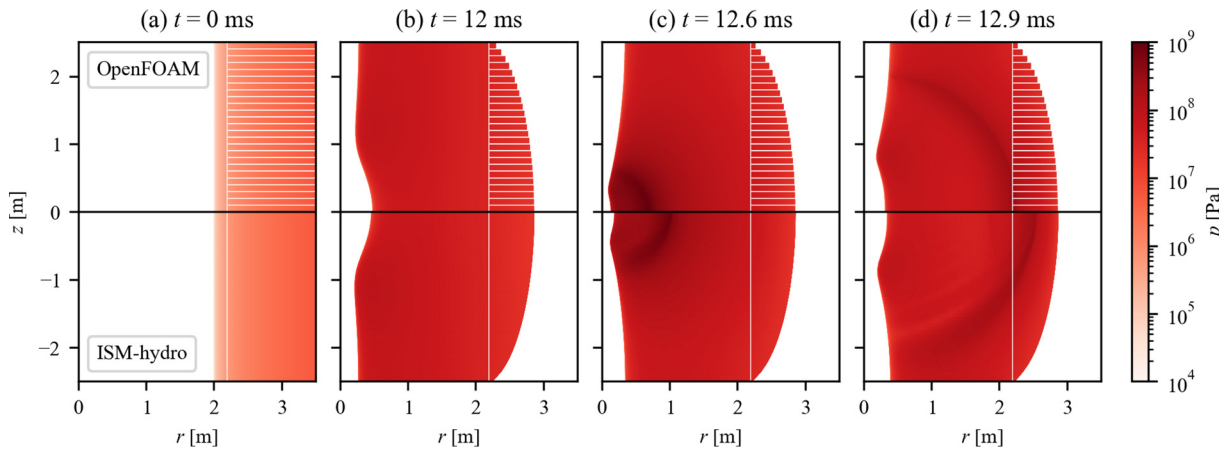


FIG. 10. Pressure field  $p$  in OpenFOAM (above equator) and ISM-hydro (below equator) at four highlighted times.

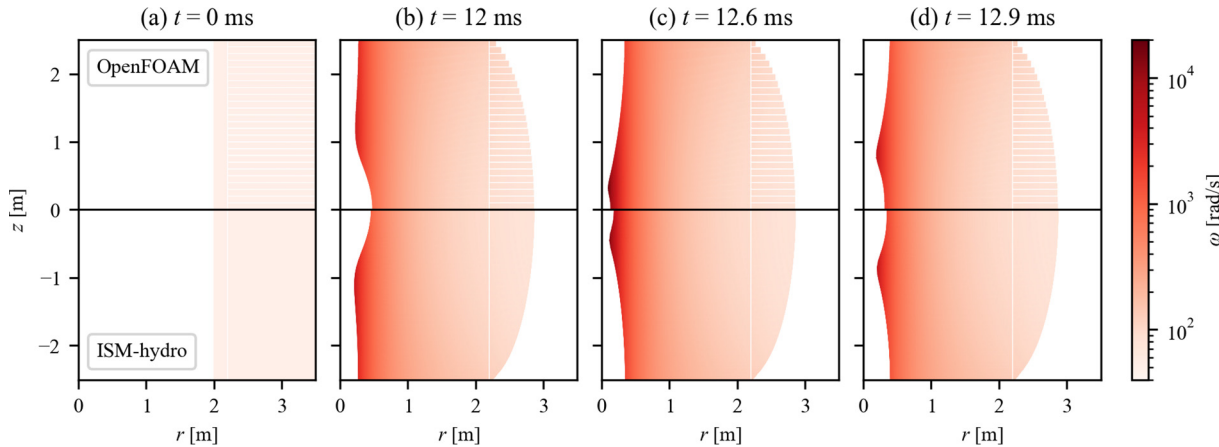


FIG. 11. Angular velocity field  $\omega$  in OpenFOAM (above equator) and ISM-hydro (below equator) at four highlighted times.

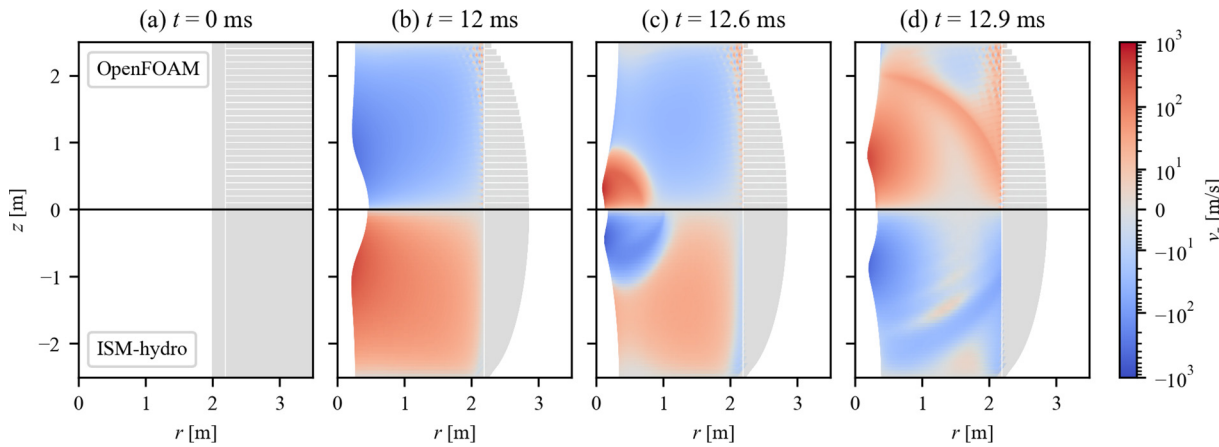
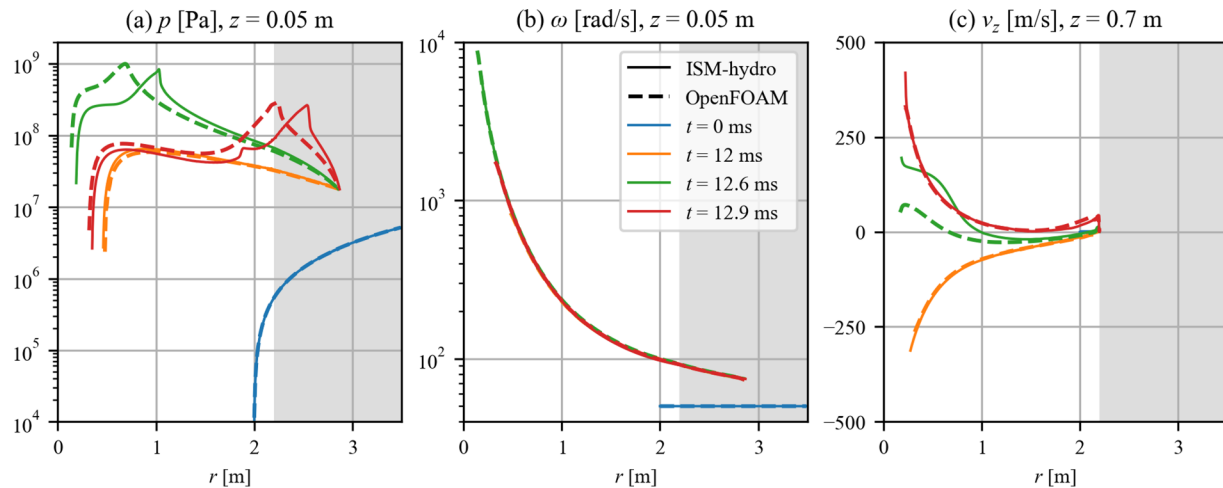


FIG. 12. Axial velocity field  $v_z$  in OpenFOAM (above equator) and ISM-hydro (below equator) at four highlighted times.



**FIG. 13.** Radial profiles of pressure  $p$ , angular velocity  $\omega$  and axial velocity  $v_z$  at four highlighted times sampled along  $z = 0.05$ ,  $z = 0.05$ , and  $z = 0.7$  m, respectively. The gray shaded area represents the region  $r \geq R_a$ .

This partition is visualized with alternating red and blue colors, corresponding to values 0 and 1 of the passive scalar, respectively. During implosion, this passive scalar is advected with the fluid flow without diffusion. The finer subdivision of vertical layers near the liner's inner surface helps to visualize the flow deep into implosion, since geometrical convergence tends to thicken vertical layers close to the axis of revolution. We then overlay a subset of ISM-hydro's vertical mesh lines  $r_j$  (black dotted lines), following an identical partition. Several conclusions can be drawn from their comparison. First, since ISM-hydro's vertical mesh lines very closely track the interfaces between colored layers during the implosion, we infer that the two codes predict very similar internal flows and the flow stays laminar. Second, it suggests that ISM-hydro's underlying assumption is valid in this case: vertical fluid layers are moderately deformed throughout the implosion without topological changes, and boundaries between these layers are well approximated by ISM-hydro's structured quadrilateral mesh. Finally, it confirms that the two codes predict the same liner shape, with a slight time delay for OpenFOAM.

Figure 10 displays the dynamics of the pressure  $p$  during implosion in both codes. At  $t = 0$  ms, the pressure distribution in the liner balances the centrifugal forces. As time progresses, the pressure increases and reaches a maximum at peak implosion near the equatorial plane. This is due to the very small equatorial turnaround radius, resulting in very large centrifugal forces. Following peak implosion, a pressure wave propagates outward.

Figure 11 shows the evolution of the angular velocity  $\omega$  in both codes. At  $t = 0$  ms, the angular velocity is initialized uniformly at  $\omega = 50$  rad/s. Due to conservation of angular momentum, the angular velocity of each fluid element increases when it approaches the axis of revolution:  $\omega \sim r^{-2}$ .

Figure 12 compares the dynamics of the axial velocity  $v_z$  in both codes. At  $t = 0$  ms, the axial velocity is equal to zero everywhere. During implosion, the fluid flows toward the equatorial plane, since shaping is achieved by pushing more liquid (higher mass flow rate) near the end plates compared to the equatorial plane. The equatorial (up-down) symmetry of the driving pressures leads to equatorial

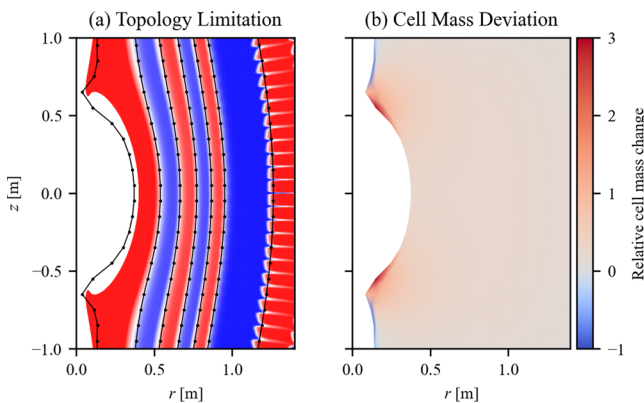
antisymmetry in the  $v_z$  field. High velocities can be observed at the same location as the pressure wave shown in Figure 10. Note that the axial velocity is essentially zero in all channels ( $r \geq R_a$ ), because of the baffles. Finer flow structures (vortices) can be observed in the OpenFOAM simulation at the channel exits, especially near the end plates where the mass flow rate is the highest.

Figure 13 displays pressure  $p$ , angular velocity  $\omega$ , and axial velocity  $v_z$  fields sampled along the horizontal planes  $z = 0.05$ ,  $z = 0.05$ , and  $z = 0.7$  m, respectively. Different lines correspond to the four highlighted times. There is excellent agreement between ISM-hydro and OpenFOAM results. After peak implosion, the pressure mismatch is essentially due to the time delay between the two codes. The difference in axial velocity at  $t = 12.6$  ms (green lines) is also related to the time delay. Figures 12(b) and 12(c) show that, around peak implosion, the axial velocity changes sign very rapidly at small radii.

The limitations of the ISM-hydro method are now explored and illustrated with strongly shaped case (iii). The value of  $P^{\max}$  in the strongly shaped case has been multiplied by a factor 1.5 compared to the shaped case. Increasing  $P^{\max}$  for a given  $\varepsilon$  (or increasing the absolute value of  $\varepsilon$  for a given  $P^{\max}$ ) tends to accentuate deformations of the vertical fluid layers.

Figure 14(a) displays the strongly shaped case before peak implosion, at  $t = 9.23$  ms. Since all inlet pressures are scaled by the same factor, the implosion is faster and turnaround occurs closer to the axis of revolution for all elevations. The two-surface waves become more pronounced and skewed toward the equatorial plane. Near peak implosion, the waves break in OpenFOAM (their crests overturn) and the liner's inner surface can no longer be described by a single-valued function of the form  $r_0(z)$  as assumed in Eq. (3). By construction, the ISM-hydro mesh cannot track this type of free surface shape.

Another limitation relates to intra-layer mass advection. ISM-hydro conserves the total mass of every vertical layer. For each layer, the mass distribution is initially uniform among the  $N_z$  cells. As the simulation progresses, if the driving gas pressures vary vertically



**FIG. 14.** The strongly shaped case before peak implosion at  $t = 9.23$  ms, zoomed-in view on the crests. (a) OpenFOAM passive scalar field and ISM-hydro mesh (subset), the initial partition is the same as in Fig. 9. The topology of the ISM-hydro mesh is not compatible with this type of free surface shape. (b) ISM-hydro relative change in cell mass  $\xi$ .

( $\varepsilon \neq 0$ ), the mass distribution will gradually deviate from uniformity for layers located at least partially outside the channels. As an example, Fig. 14(b) displays the relative change in cell mass  $\xi$  for the strongly shaped case at  $t = 9.23$  ms, where  $\xi$  is defined for all indices  $j + 1/2, k + 1/2$  as

$$\xi_{j+\frac{1}{2},k+\frac{1}{2}} = \frac{m_{j+\frac{1}{2},k+\frac{1}{2}} - m_{j+\frac{1}{2},k+\frac{1}{2}}|_{t=0}}{m_{j+\frac{1}{2},k+\frac{1}{2}}|_{t=0}}. \quad (43)$$

In some extreme cases with pronounced flows in the axial direction, one or more cell masses may approach zero ( $\xi = -1$ ) and lead to numerical instabilities. Different numerical strategies can be employed to circumvent this limitation, such as a careful choice of the initial mesh radial distribution, the merging of adjacent vertical layers if a cell mass drops below some threshold, and the use of cell mass or cell radial size limiters. In general, the topology and mass related limitations illustrated in Fig. 14 can arise for mesh lines and cells located not only at the surface, but in the bulk of the fluid as well.

#### IV. CONCLUSION

ISM-hydro is an interface tracking, finite volume code solving the Euler equations for a rotating compressible fluid in an axisymmetric setting. The code is a novel implementation of the mixed Lagrangian–Eulerian approach and, as such, it inherits both its advantages and limitations. The first of these advantages is that ISM-hydro is naturally designed to accurately track the free surface of a moving fluid. This is especially important when modeling an MTF system with plasma, since the free surface of the liner determines the shape and boundary conditions for the magnetized plasma target.

The other advantage of our code over more traditional fluid dynamics software is speed. We show that even coarse resolution ISM-hydro simulations of liquid liner implosions compare very well against equivalent OpenFOAM simulations and only require run time on the order of one minute on a single core. As resolution in both codes is increased, their solutions converge very closely. The agreement extends beyond prediction of the free surfaces, with almost identical internal flow patterns between the two codes.

In addition, the ISM-hydro finite volume discretization satisfies an exact balance of kinetic energy—a property inherent to the continuous Euler equations. If the fluid internal energy is incorporated into the numerical scheme, such a property leads to the exact discrete analogue of the energy conservation law. Reproducing the conservation law in discrete form improves the physical fidelity of the numerical scheme by imposing more constraints.

The resulting ISM-hydro scheme has first order accuracy in space and uses second order explicit integration in time (Runge–Kutta second order method). Artificial viscosity is introduced for stability of the numerical scheme. The first order of spatial accuracy is sufficient for our purpose of simulating the liner’s implosion trajectory. We note that the scheme is not specifically designed to simulate shocks; however, the shock propagation is well captured in the presented test cases with a very good quantitative comparison against OpenFOAM.

The presented method has some limitations by construction. Its underlying structured quadrilateral mesh can only represent free surfaces and internal bounding lines that can be expressed mathematically as a single-valued function mapping from  $z$  to  $r$ . Some scenarios with large distortions of the vertical layers or significant intra-layer mass advection may not be predicted accurately and can result in numerical instabilities. Various numerical strategies can be employed to extend the range of applicability of the method, trading accuracy in the predictions for numerical robustness.

Ultimately, the ISM-hydro method can be extended to include thermal and magnetohydrodynamic effects and be consistently coupled with a plasma model for MTF simulations.

#### ACKNOWLEDGMENTS

We are very grateful to our colleagues Colin McNally, Victoria Suponitsky, and Meritt Reynolds for their valuable comments and numerous suggestions that have greatly improved this work.

This work was supported by funding from the Government of Canada through its Strategic Innovation Fund (Agreement No. 811-811346). The funding source had no involvement in the study design; the collection, analysis and interpretation of data; the writing of the report; the decision to submit the article for publication.

#### AUTHOR DECLARATIONS

##### Conflict of Interest

The authors have no conflicts to disclose.

##### Author Contributions

**Ivan V. Khalzov:** Conceptualization (equal); Formal analysis (equal); Investigation (equal); Methodology (lead); Software (equal); Validation (equal); Visualization (equal); Writing – original draft (equal); Writing – review & editing (equal). **Daymon Krotez:** Data curation (lead); Formal analysis (equal); Investigation (equal); Software (equal); Validation (equal); Visualization (equal); Writing – review & editing (equal). **Raphaël Ségas:** Conceptualization (equal); Formal analysis (equal); Investigation (equal); Project administration (lead); Software (equal); Supervision (lead); Validation (equal); Visualization (equal); Writing – original draft (equal); Writing – review & editing (equal).

## DATA AVAILABILITY

The data that support the findings of this study are openly available in Zenodo at <https://doi.org/10.5281/zenodo.8423698>, Ref. 14 and in Mendeley Data at <https://doi.org/10.17632/x6cg77vw9s.1>, Ref. 20.

## APPENDIX A: REDUCTION OF CONTINUOUS EQUATIONS TO FINITE VOLUME FORM

Here, we demonstrate how the discrete equations (5) are obtained from the original continuous equations (1). Every equation in system (1) has the general form

$$\dot{a} = -\nabla \cdot (a\mathbf{v}) + g. \quad (\text{A1})$$

We introduce the control volume integral of quantity  $a$ ; for example, if the control volume corresponds to a mesh cell (as for density  $\rho$ ), then

$$A_{j+\frac{1}{2}k+\frac{1}{2}} \leftarrow \int_{V_{j+\frac{1}{2}k+\frac{1}{2}}} a \, dV.$$

We calculate its time derivative, taking into account the motion of the control volume, substituting Eq. (A1) and applying Gauss's divergence theorem

$$\begin{aligned} \frac{dA_{j+\frac{1}{2}k+\frac{1}{2}}}{dt} &\leftarrow \int_{\partial V_{j+\frac{1}{2}k+\frac{1}{2}}} a \mathbf{v}_\Gamma \cdot d\mathbf{S} + \int_{V_{j+\frac{1}{2}k+\frac{1}{2}}} (-\nabla \cdot (a\mathbf{v}) + g) \, dV \\ &= \int_{\partial V_{j+\frac{1}{2}k+\frac{1}{2}}} a (\mathbf{v}_\Gamma - \mathbf{v}) \cdot d\mathbf{S} + \int_{V_{j+\frac{1}{2}k+\frac{1}{2}}} g \, dV, \end{aligned} \quad (\text{A2})$$

where  $\partial V_{j+1/2k+1/2}$  denotes the boundary surface of the control volume,  $d\mathbf{S} \equiv \mathbf{n} \, dS$  is the area element of this surface combined with the unit normal vector  $\mathbf{n}$  pointing outward, and  $\mathbf{v}_\Gamma$  is the velocity of this surface. For our radially Lagrangian mesh, the left and right boundaries of the cell associated with vertical mesh lines are impenetrable (material) boundaries for the fluid flow  $\mathbf{v}$ , so the following condition is satisfied locally along every vertical mesh line  $r_j(t, z)$  (this is also true for the lines with half-integer index  $r_{j+1/2}(t, z)$  bounding corresponding control volumes)

$$(\mathbf{v}_\Gamma - \mathbf{v}) \cdot \mathbf{n} = 0 \quad \text{along every } r_j(t, z).$$

At the cell's top and bottom boundaries, since all horizontal mesh lines are steady, we have

$$\mathbf{v}_\Gamma \cdot \mathbf{n} = 0 \quad \text{along every } z_k.$$

Therefore, the only contributions to the surface integral in Eq. (A2) come from the top and bottom horizontal boundaries, namely,

$$\int_{\partial V_{j+\frac{1}{2}k+\frac{1}{2}}} a (\mathbf{v}_\Gamma - \mathbf{v}) \cdot d\mathbf{S} = \int_{r_{jk}}^{r_{j+1k}} (av_z)|_{z=z_k} 2\pi r dr - \int_{r_{jk+1}}^{r_{j+1k+1}} (av_z)|_{z=z_{k+1}} 2\pi r dr.$$

Defining the discrete axial flux and the source term as

$$\begin{aligned} \int_{r_{jk}}^{r_{j+1k}} (av_z)|_{z=z_k} 2\pi r dr &\Rightarrow q_{j+\frac{1}{2}k}^A, \\ \int_{V_{j+\frac{1}{2}k+\frac{1}{2}}} g \, dV &\Rightarrow G_{j+\frac{1}{2}k+\frac{1}{2}}^A, \end{aligned}$$

and noting that the full and partial time derivatives are identical for a univariate function (time dependence only), we can rewrite Eq. (A2) as

$$\dot{A}_{j+\frac{1}{2}k+\frac{1}{2}} = q_{j+\frac{1}{2}k}^A - q_{j+\frac{1}{2}k+1}^A + G_{j+\frac{1}{2}k+\frac{1}{2}}^A, \quad (\text{A3})$$

which is exactly the form of the equations in system (5)

An important corollary of Eq. (A3) is the discrete form of the fluid velocity divergence. Indeed, Eq. (A1) is satisfied identically if we choose

$$a = 1, \quad g = \nabla \cdot \mathbf{v}.$$

With this choice, Eq. (A3) gives the time derivative of the cell volume

$$\dot{V}_{j+\frac{1}{2}k+\frac{1}{2}} = q_{j+\frac{1}{2}k}^V - q_{j+\frac{1}{2}k+1}^V + (\nabla \cdot \mathbf{v})_{j+\frac{1}{2}k+\frac{1}{2}} V_{j+\frac{1}{2}k+\frac{1}{2}}, \quad (\text{A4})$$

where the last term, containing the discrete velocity divergence, comes from the approximation

$$\int_{V_{j+\frac{1}{2}k+\frac{1}{2}}} (\nabla \cdot \mathbf{v}) \, dV \Rightarrow G_{j+\frac{1}{2}k+\frac{1}{2}}^V = (\nabla \cdot \mathbf{v})_{j+\frac{1}{2}k+\frac{1}{2}} V_{j+\frac{1}{2}k+\frac{1}{2}}.$$

Rearranging the terms in Eq. (A4), we obtain

$$(\nabla \cdot \mathbf{v})_{j+\frac{1}{2}k+\frac{1}{2}} = \frac{\dot{V}_{j+\frac{1}{2}k+\frac{1}{2}} + q_{j+\frac{1}{2}k+1}^V - q_{j+\frac{1}{2}k}^V}{V_{j+\frac{1}{2}k+\frac{1}{2}}}. \quad (\text{A5})$$

The volume of the cell, given by Eqs. (11) or (36), only changes due to the radial motion of its vertical boundaries

$$\dot{V}_{j+\frac{1}{2}k+\frac{1}{2}} = \dot{r}_{j+1k+\frac{1}{2}} S_{j+1k+\frac{1}{2}} - \dot{r}_{jk+\frac{1}{2}} S_{jk+\frac{1}{2}}, \quad (\text{A6})$$

where the areas of the corresponding vertical cell boundaries are determined by Eqs. (17a) or (35). The "volume flux" through the horizontal cell boundaries can be approximated using the discrete axial velocity as

$$\int_{r_{jk}}^{r_{j+1k}} v_z|_{z=z_k} 2\pi r dr \Rightarrow q_{j+\frac{1}{2}k}^V = v_{zj+\frac{1}{2}k} S_{j+\frac{1}{2}k}, \quad S_{j+\frac{1}{2}k} = \pi(r_{j+1k}^2 - r_{jk}^2). \quad (\text{A7})$$

Substituting Eqs. (A6) and (A7) into Eq. (A5), we obtain the discrete form of the velocity divergence as in Eq. (22).

## APPENDIX B: FLUXES AND SHEAR TERMS

Here, we outline the derivation of the RHS terms in system (5), namely, the fluxes and the shear terms in the radial velocity and axial pressure.

Using Gauss's divergence theorem, the full pressure force in Eq. (5c) is given as

$$f_{zj+\frac{1}{2}k}^p \Leftarrow - \int_{V_{j+\frac{1}{2}k}} p'_z dV = - \int_{V_{j+\frac{1}{2}k}} \nabla \cdot (p \mathbf{e}_z) dV = - \int_{\partial V_{j+\frac{1}{2}k}} p dS_z, \quad (B1)$$

i.e., it is expressed as the pressure integrated over the horizontal elements of the surface bounding the control volume. In the above equation, we used the identities

$$\nabla \cdot (p \mathbf{e}_z) = \nabla p \cdot \mathbf{e}_z + p \nabla \cdot \mathbf{e}_z = p'_z, \quad \nabla \cdot \mathbf{e}_z = 0,$$

where  $\mathbf{e}_z$  is the unit vector in the axial direction. The surface integral in Eq. (B1) can be discretized assuming constant values of pressure along different parts of the control volume surface

$$\begin{aligned} f_{zj+\frac{1}{2}k}^p &= p_{j+\frac{1}{2}k-\frac{1}{2}} \pi \left( r_{j+1k-\frac{1}{2}}^2 - r_{jk-\frac{1}{2}}^2 \right) - p_{j+\frac{1}{2}k+\frac{1}{2}} \pi \left( r_{j+1k+\frac{1}{2}}^2 - r_{jk+\frac{1}{2}}^2 \right) \\ &+ p_{jk-\frac{1}{2}} \pi \left( r_{jk-\frac{1}{2}}^2 - r_{jk}^2 \right) + p_{jk+\frac{1}{2}} \pi \left( r_{jk}^2 - r_{jk+\frac{1}{2}}^2 \right) \\ &+ p_{j+1k-\frac{1}{2}} \pi \left( r_{j+1k}^2 - r_{j+1k-\frac{1}{2}}^2 \right) + p_{j+1k+\frac{1}{2}} \pi \left( r_{j+1k+\frac{1}{2}}^2 - r_{j+1k}^2 \right). \end{aligned} \quad (B2)$$

Here, we define the pressure value at every side face (vertical boundary) of the control volume as a weighted average between two fluid cells sharing that face

$$p_{jk+\frac{1}{2}} = w_{jk+\frac{1}{2}}^r p_{j-\frac{1}{2}k+\frac{1}{2}} + w_{jk+\frac{1}{2}}^l p_{j+\frac{1}{2}k+\frac{1}{2}}, \quad w_{jk+\frac{1}{2}}^r + w_{jk+\frac{1}{2}}^l = 1. \quad (B3)$$

Note that the weights in Eq. (B3) are the same as those defined in Eq. (28), but in the present derivation, they are introduced as free parameters that have yet to be determined. Equation (B2) identically satisfies the pressure force balance condition (24) since for adjacent control volumes the corresponding force terms enter with opposite signs and, therefore, cancel when all forces are summed up. Substituting Eq. (B3) into Eq. (B2) and rearranging the terms, we obtain the full axial pressure force given by Eq. (16b) with Eq. (31).

Now we consider a discrete analogue of the kinetic energy balance (25). The discrete form of the total kinetic energy is

$$\begin{aligned} \int_V \frac{1}{2} \rho \mathbf{v}^2 dV &\Rightarrow \\ E_{kin} &= \sum_{j,k} \frac{1}{2} \left( m_{jk+\frac{1}{2}} v_{rjk+\frac{1}{2}}^2 + m_{j+\frac{1}{2}k} v_{zj+\frac{1}{2}k}^2 + m_{jk+\frac{1}{2}} \omega_{jk+\frac{1}{2}}^2 r_{jk+\frac{1}{2}}^2 \right) \\ &= \sum_{j,k} \frac{1}{2} \left( \frac{M_{rjk+\frac{1}{2}}^2}{m_{jk+\frac{1}{2}}} + \frac{M_{zj+\frac{1}{2}k}^2}{m_{j+\frac{1}{2}k}} + \frac{L_{jk+\frac{1}{2}}^2}{m_{jk+\frac{1}{2}}} \right). \end{aligned} \quad (B4)$$

Here and below, the summation is performed over the appropriate full range of indices  $j$  and  $k$ . The time derivative of  $E_{kin}$  is

$$\begin{aligned} \dot{E}_{kin} &= \sum_{j,k} \left( v_{rjk+\frac{1}{2}} \dot{M}_{rjk+\frac{1}{2}} - \frac{\dot{m}_{jk+\frac{1}{2}} v_{rjk+\frac{1}{2}}^2}{2} + v_{zj+\frac{1}{2}k} \dot{M}_{zj+\frac{1}{2}k} - \frac{\dot{m}_{j+\frac{1}{2}k} v_{zj+\frac{1}{2}k}^2}{2} + \omega_{jk+\frac{1}{2}} \dot{L}_{jk+\frac{1}{2}} - \frac{\dot{m}_{jk+\frac{1}{2}} \omega_{jk+\frac{1}{2}}^2 r_{jk+\frac{1}{2}}^2}{2} - m_{jk+\frac{1}{2}} \omega_{jk+\frac{1}{2}}^2 r_{jk+\frac{1}{2}} \dot{r}_{jk+\frac{1}{2}} \right) \\ &= \sum_{j,k} \left( v_{rjk+\frac{1}{2}} f_{rjk+\frac{1}{2}}^p + v_{zj+\frac{1}{2}k} f_{zj+\frac{1}{2}k}^p \right) + \sum_{j,k} \left( v_{rjk+\frac{1}{2}} \left( q_{jk}^{M_r} - q_{jk+1}^{M_r} \right) - \frac{v_{rjk+\frac{1}{2}}^2}{2} \left( q_{jk}^m - q_{jk+1}^m \right) \right) \\ &+ \sum_{j,k} \left( v_{zj+\frac{1}{2}k} \left( q_{j+\frac{1}{2}k-\frac{1}{2}}^{M_z} - q_{j+\frac{1}{2}k+\frac{1}{2}}^{M_z} \right) - \frac{v_{zj+\frac{1}{2}k}^2}{2} \left( q_{j+\frac{1}{2}k-\frac{1}{2}}^m - q_{j+\frac{1}{2}k+\frac{1}{2}}^m \right) \right) \\ &+ \sum_{j,k} \left( \omega_{jk+\frac{1}{2}} \left( q_{jk}^L - q_{jk+1}^L \right) - \frac{\omega_{jk+\frac{1}{2}}^2 r_{jk+\frac{1}{2}}^2}{2} \left( q_{jk}^m - q_{jk+1}^m \right) + m_{jk+\frac{1}{2}} \omega_{jk+\frac{1}{2}}^2 r_{jk+\frac{1}{2}} \delta v_{rjk+\frac{1}{2}} \right), \end{aligned} \quad (B5)$$

where we substituted the time derivatives of the momenta from Eqs. (5b)–(5d) and assumed that the masses of the control volumes change due to the corresponding mass fluxes, similar to Eq. (5a). We then regrouped all the terms into four distinct sums in the final expression of Eq. (B5). The first, second, and third sums contain all the terms scaling as  $p$ ,  $v_r^2 v_z$ , and  $v_z^3$ , respectively, while the last sum contains all the terms depending on  $\omega$ . According to Eq. (25), only pressure terms can contribute to the final result; therefore, all sums but the first one must be equal to zero. This gives us the conditions for determining consistent expressions for the radial velocity shear term and corresponding fluxes.

Substituting the general form of radial velocity (15) and the components of pressure force (16) with (31) into the first sum and rearranging terms, we obtain

$$\begin{aligned} &\sum_{j,k} \left( v_{rjk+\frac{1}{2}} f_{rjk+\frac{1}{2}}^p + v_{zj+\frac{1}{2}k} f_{zj+\frac{1}{2}k}^p \right) \\ &= \sum_{j,k} \left( -\dot{r}_{jk+\frac{1}{2}} S_{jk+\frac{1}{2}} (p_{j+\frac{1}{2}k+\frac{1}{2}} - p_{j-\frac{1}{2}k+\frac{1}{2}}) - v_{zj+\frac{1}{2}k} S_{j+\frac{1}{2}k} (p_{j+\frac{1}{2}k+\frac{1}{2}} - p_{j+\frac{1}{2}k-\frac{1}{2}}) \right) \\ &+ \sum_{j,k} \left( \delta v_{rjk+\frac{1}{2}} f_{rjk+\frac{1}{2}}^p + v_{zj+\frac{1}{2}k} \delta f_{zj+\frac{1}{2}k}^p \right) \\ &= \sum_{j,k} p_{j+\frac{1}{2}k+\frac{1}{2}} (\nabla \cdot \mathbf{v})_{j+\frac{1}{2}k+\frac{1}{2}} V_{j+\frac{1}{2}k+\frac{1}{2}} \\ &+ \sum_{j,k} \Delta p_{jk+\frac{1}{2}} \left( -\delta v_{rjk+\frac{1}{2}} S_{jk+\frac{1}{2}} + v_{zj+\frac{1}{2}k}^b \pi \left( r_{jk+\frac{1}{2}}^2 - r_{jk}^2 \right) \right. \\ &\left. + v_{zj+\frac{1}{2}k}^t \pi \left( r_{jk+1}^2 - r_{jk+\frac{1}{2}}^2 \right) \right), \end{aligned} \quad (B6)$$

where we introduced the discrete velocity divergence, as in Eq. (22), and axial velocities  $v_{zjk+1/2}^b$  and  $v_{zjk+1/2}^t$ , as in Eq. (27). The resulting form of Eq. (B6) gives us a discrete analogue of the RHS of Eq. (25) with the velocity divergence in the bulk of the fluid domain, provided that the last sum in Eq. (B6) is zero. This condition leads to Eq. (26)—the discrete expression for the radial velocity shear term.

To zero out the second sum in Eq. (B5), we assume the most general form of the radial momentum flux with linear dependence on the radial velocity

$$q_{jk}^M = B_{jk-\frac{1}{2}} v_{rjk-\frac{1}{2}} + C_{jk+\frac{1}{2}} v_{rjk+\frac{1}{2}}. \quad (\text{B7})$$

Substituting this into the second sum in Eq. (B5) and rearranging terms, we obtain the equation

$$0 = \sum_{j,k} \left( v_{rjk-\frac{1}{2}} v_{rjk+\frac{1}{2}} (B_{jk-\frac{1}{2}} - C_{jk+\frac{1}{2}}) + v_{rjk+\frac{1}{2}}^2 \left( C_{jk+\frac{1}{2}} - B_{jk+\frac{1}{2}} - \frac{q_{jk}^m}{2} + \frac{q_{jk+1}^m}{2} \right) \right),$$

which has solution

$$B_{jk-\frac{1}{2}} = C_{jk+\frac{1}{2}} = \frac{q_{jk}^m}{2}. \quad (\text{B8})$$

Equation (B7) with coefficients (B8) gives us the radial momentum flux as in Eq. (29a).

The third sum in Eq. (B5) is handled in the same way, leading to the axial momentum flux as in Eq. (29b).

Finally, to zero out the last sum in Eq. (B5), we assume the following form of the angular momentum flux

$$q_{jk}^L = \frac{D_{jk}}{2} (\omega_{jk-\frac{1}{2}} + \omega_{jk+\frac{1}{2}}). \quad (\text{B9})$$

$$m_{j+\frac{1}{2}k} = \frac{w_{jk-\frac{1}{2}}^r m_{jk-\frac{1}{2}} (r_{jk}^2 - r_{jk-\frac{1}{2}}^2) + w_{jk+\frac{1}{2}}^r m_{jk+\frac{1}{2}} (r_{jk+\frac{1}{2}}^2 - r_{jk}^2)}{(r_{jk+\frac{1}{2}}^2 - r_{jk-\frac{1}{2}}^2)} + \frac{w_{j+1k-\frac{1}{2}}^l m_{j+1k-\frac{1}{2}} (r_{j+1k-\frac{1}{2}}^2 - r_{j+1k-\frac{1}{2}}^2) + w_{j+1k+\frac{1}{2}}^l m_{j+1k+\frac{1}{2}} (r_{j+1k+\frac{1}{2}}^2 - r_{j+1k}^2)}{(r_{j+1k+\frac{1}{2}}^2 - r_{j+1k-\frac{1}{2}}^2)}. \quad (\text{B14})$$

Finally, we sum up both sides of the above equation over all indices  $j$  and  $k$  (over the whole fluid domain) to obtain the total fluid mass

$$\sum_{j,k} m_{j+\frac{1}{2}k} = \sum_{j,k} m_{jk+\frac{1}{2}} \left( \frac{r_{jk+\frac{1}{2}}^2 - r_{jk}^2}{r_{jk+\frac{1}{2}}^2 - r_{jk-\frac{1}{2}}^2} + \frac{r_{jk+1}^2 - r_{jk+\frac{1}{2}}^2}{r_{jk+\frac{3}{2}}^2 - r_{jk+\frac{1}{2}}^2} \right).$$

In order to have the total fluid mass on the RHS of this equation, the expression in brackets must be equal to 1 for each  $m_{jk+1/2}$  term, i.e.,

$$\frac{r_{jk+\frac{1}{2}}^2 - r_{jk}^2}{r_{jk+\frac{1}{2}}^2 - r_{jk-\frac{1}{2}}^2} + \frac{r_{jk+1}^2 - r_{jk+\frac{1}{2}}^2}{r_{jk+\frac{3}{2}}^2 - r_{jk+\frac{1}{2}}^2} = 1, \quad (\text{B15})$$

which is an equation for determining  $r_{jk}$ . Assuming that  $r_{jk}$  only depends on the position of the neighboring points,  $r_{jk+1/2}$  and  $r_{jk-1/2}$ , we obtain the general relation from Eq. (B15),

Then, the last sum in Eq. (B5) leads to

$$0 = D_{jk} - D_{jk+1} - r_{jk+\frac{1}{2}}^2 (q_{jk}^m - q_{jk+1}^m) + \frac{m_{jk+\frac{1}{2}}}{\Delta z} \left( v_{zjk+\frac{1}{2}}^b (r_{jk+\frac{1}{2}}^2 - r_{jk}^2) + v_{zjk+\frac{1}{2}}^t (r_{jk+1}^2 - r_{jk+\frac{1}{2}}^2) \right). \quad (\text{B10})$$

Since at each level  $z=z_k$  all the fluxes must be proportional to the axial velocity  $v_z$ , we can split Eq. (B10) into two independent equations

$$D_{jk} = r_{jk+\frac{1}{2}}^2 q_{jk}^m - \frac{m_{jk+\frac{1}{2}} v_{zjk+\frac{1}{2}}^b}{\Delta z} (r_{jk+\frac{1}{2}}^2 - r_{jk}^2), \quad (\text{B11a})$$

$$D_{jk+1} = r_{jk+\frac{1}{2}}^2 q_{jk+1}^m + \frac{m_{jk+\frac{1}{2}} v_{zjk+\frac{1}{2}}^t}{\Delta z} (r_{jk+1}^2 - r_{jk+\frac{1}{2}}^2). \quad (\text{B11b})$$

Reindexing Eq. (B11b), we can remove  $D_{jk}$  and obtain

$$q_{jk}^m = \frac{m_{jk-\frac{1}{2}} v_{zjk-\frac{1}{2}}^t (r_{jk}^2 - r_{jk-\frac{1}{2}}^2) + m_{jk+\frac{1}{2}} v_{zjk+\frac{1}{2}}^b (r_{jk+\frac{1}{2}}^2 - r_{jk}^2)}{\Delta z (r_{jk+\frac{1}{2}}^2 - r_{jk-\frac{1}{2}}^2)}. \quad (\text{B12})$$

The total mass flux through level  $z=z_k$  must be the same whether it is written in terms of  $q_{jk}^m$  or in terms of  $q_{j+1/2k}^m$ , i.e.,

$$\sum_j q_{jk}^m = \sum_j q_{j+\frac{1}{2}k}^m. \quad (\text{B13})$$

Using Eqs. (27) and (23), the axial velocities in Eq. (B12) can be expressed as functions of mass fluxes  $q_{j+1/2k}^m$ . Substituting Eq. (B12) into Eq. (B13) and treating each  $q_{j+1/2k}^m$  term as independent, we arrive at

$$r_{jk}^2 = \beta_j r_{jk-1/2}^2 + (1 - \beta_j) r_{jk+1/2}^2,$$

where  $\beta_j$  is an arbitrary constant. We choose  $\beta_j = 1/2$  since this provides the best approximation order for a mesh uniform in  $z$ , leading to Eq. (18). With this expression for  $r_{jk}^2$ , Eq. (B14) becomes

$$m_{j+\frac{1}{2}k} = \frac{1}{2} (w_{jk-\frac{1}{2}}^r m_{jk-\frac{1}{2}} + w_{jk+\frac{1}{2}}^r m_{jk+\frac{1}{2}} + w_{j+1k-\frac{1}{2}}^l m_{j+1k-\frac{1}{2}} + w_{j+1k+\frac{1}{2}}^l m_{j+1k+\frac{1}{2}}). \quad (\text{B16})$$

Here, the mass on the LHS can only depend on the masses of the two adjacent mesh cells in the same vertical layer,  $m_{j+1/2k-1/2}$  and  $m_{j+1/2k+1/2}$ . This is satisfied if the terms inside the brackets obey the following condition for all  $k$ ,

$$w_{jk+\frac{1}{2}}^r m_{jk+\frac{1}{2}} + w_{j+1k+\frac{1}{2}}^l m_{j+1k+\frac{1}{2}} = m_{j+\frac{1}{2}k+\frac{1}{2}}.$$

In other words, the mass of a mesh cell  $(j + 1/2, k + 1/2)$  is divided between the left  $(j, k + 1/2)$  and right  $(j + 1, k + 1/2)$  control volumes

$$m_{j+\frac{1}{2}k+\frac{1}{2}} = m_{j+\frac{1}{2}k+\frac{1}{2}}^l + m_{j+\frac{1}{2}k+\frac{1}{2}}^r, \quad (B17a)$$

$$m_{jk+\frac{1}{2}} = m_{j+\frac{1}{2}k+\frac{1}{2}}^l + m_{j-\frac{1}{2}k+\frac{1}{2}}^r, \quad (B17b)$$

$$w_{jk+\frac{1}{2}}^r = \frac{m_{j+\frac{1}{2}k+\frac{1}{2}}^r}{m_{jk+\frac{1}{2}}}, \quad w_{jk+\frac{1}{2}}^l = \frac{m_{j-\frac{1}{2}k+\frac{1}{2}}^r}{m_{jk+\frac{1}{2}}}. \quad (B17c)$$

This division of a mesh cell is arbitrary; for the best approximation order, we choose division into equal masses

$$m_{j+\frac{1}{2}k+\frac{1}{2}}^l = m_{j+\frac{1}{2}k+\frac{1}{2}}^r = \frac{m_{j+\frac{1}{2}k+\frac{1}{2}}}{2}.$$

As a result, Eqs. (B17b) and (B16) lead to control volume masses definition (12), Eq. (B17c) gives weights definition (28), Eq. (B12) gives the mass flux in Eq. (30a), and Eq. (B9) with Eq. (B11a) lead to the angular momentum flux in Eq. (29c).

## APPENDIX C: LAGRANGIAN NATURE OF THE ONE-DIMENSIONAL EQUATIONS OF MOTION

Here, we show that the one-dimensional equations of fluid motion (37) inside the rotor channels can be derived using the Lagrangian formalism. We introduce the Lagrangian function as (for simplicity indices  $k$  are omitted)

$$\mathcal{L} \equiv E_{kin} - U = \sum_j \frac{m_j}{2} \left( \dot{r}_j^2 + \omega_j^2 r_j^2 \right) - \sum_j U_{j+\frac{1}{2}},$$

where  $U_{j+1/2}$  is the internal energy of the fluid cell  $j + 1/2$ . Treating  $r_j$  as a generalized coordinate, and  $\dot{r}_j$  and  $\omega_j$  as generalized velocities, we obtain the Euler-Lagrange equations of motion

$$\begin{aligned} \frac{d}{dt} \left( \frac{\partial \mathcal{L}}{\partial \dot{r}_j} \right) &= \frac{\partial \mathcal{L}}{\partial r_j}, \\ \frac{d}{dt} \left( \frac{\partial \mathcal{L}}{\partial \omega_j} \right) &= 0. \end{aligned}$$

After substitution of  $\mathcal{L}$ , we have

$$\frac{d}{dt} (m_j \dot{r}_j) = m_j \omega_j^2 r_j - \frac{\partial U}{\partial r_j}, \quad (C1a)$$

$$\frac{d}{dt} (m_j \omega_j r_j^2) = 0. \quad (C1b)$$

The total change of internal energy due to fluid cells motion is related to the work done by the pressure of each cell

$$dU = - \sum_j p_{j+\frac{1}{2}} dV_{j+\frac{1}{2}}.$$

Only two terms from this sum (with the cell volumes depending on  $r_j$ ) contribute to the partial derivative of internal energy

$$\frac{\partial U}{\partial r_j} = -p_{j-\frac{1}{2}} \frac{\partial V_{j-\frac{1}{2}}}{\partial r_j} - p_{j+\frac{1}{2}} \frac{\partial V_{j+\frac{1}{2}}}{\partial r_j} = S_j (p_{j+\frac{1}{2}} - p_{j-\frac{1}{2}}), \quad (C2)$$

since

$$dV_{j-\frac{1}{2}} = -dV_{j+\frac{1}{2}} = S_j dr_j.$$

Substituting Eq. (C2) in Eq. (C1a) and noting that each mass  $m_j$  is constant, we obtain Eq. (37).

## REFERENCES

- <sup>1</sup>M. Laberge, "Magnetized target fusion with a spherical tokamak," *J. Fusion Energy* **38**, 199–203 (2019).
- <sup>2</sup>V. Suponitsky, I. V. Khalzov, and E. J. Avital, "Magnetohydrodynamics solver for a two-phase free surface flow developed in OpenFOAM," *Fluids* **7**, 210 (2022).
- <sup>3</sup>N. S. Mangione, H. Wu, C. Preston, A. M. D. Lee, S. Entezami, R. Ségas, P. W. Forsyinski, and V. Suponitsky, "Shape manipulation of a rotating liquid liner imploded by arrays of pneumatic pistons: Experimental and numerical study," *Fusion Eng. Des.* **198**, 114087 (2024).
- <sup>4</sup>E. Audusse, "A multilayer Saint-Venant model: Derivation and numerical validation," *Discrete Contin. Dyn. Syst.-B.* **5**, 189–214 (2005).
- <sup>5</sup>S. Popinet, "A vertically-Lagrangian, non-hydrostatic, multilayer model for multiscale free-surface flows," *J. Comput. Phys.* **418**, 109609 (2020).
- <sup>6</sup>N. Ali, Z. Asghar, M. Sajid, and F. Abbas, "A hybrid numerical study of bacteria gliding on a shear rate-dependent slime," *Physica A* **535**, 122435 (2019).
- <sup>7</sup>Z. Asghar, R. A. Shah, and N. Ali, "A numerical framework for modeling the dynamics of micro-organism movement on Carreau-Yasuda layer," *Soft Comput.* **27**, 8525–8539 (2023).
- <sup>8</sup>T. E. Tezduyar, "Interface-tracking and interface-capturing techniques for finite element computation of moving boundaries and interfaces," *Comput. Methods Appl. Mech. Eng.* **195**, 2983–3000 (2006).
- <sup>9</sup>Ž. Tuković and H. Jasak, "A moving mesh finite volume interface tracking method for surface tension dominated interfacial fluid flow," *Comput. Fluids* **55**, 70–84 (2012).
- <sup>10</sup>R. H. Cole, *Underwater Explosions* (Princeton University Press, 1948).
- <sup>11</sup>J. Campbell and R. Vignjevic, "Artificial viscosity methods for modelling shock wave propagation," in *Predictive Modeling of Dynamic Processes: A Tribute to Professor Klaus Thoma*, edited by S. Hiermaier (Springer US, Boston, MA, 2009), pp. 349–365.
- <sup>12</sup>J. Albright and M. Shashkov, "Locally adaptive artificial viscosity strategies for Lagrangian hydrodynamics," *Comput. Fluids* **205**, 104580 (2020).
- <sup>13</sup>L. G. Margolin and N. M. Lloyd-Ronning, "Artificial viscosity—Then and now," *Mecanica* **58**, 1039–1052 (2023).
- <sup>14</sup>I. V. Khalzov, D. Krotez, and R. Ségas (2023). "ISM-hydro: An interface tracking, finite volume code for modeling axisymmetric implosion of a rotating liquid metal liner with free surface," Zenodo, V. 1.0.0, Dataset <https://doi.org/10.5281/zenodo.8423698>
- <sup>15</sup>C. W. Hirt and B. D. Nichols, "Volume of fluid (VOF) method for the dynamics of free boundaries," *J. Comput. Phys.* **39**, 201–225 (1981).
- <sup>16</sup>O. Ubbink, "Numerical prediction of two fluid systems with sharp interfaces," Ph.D. thesis (Imperial College London, 1997).
- <sup>17</sup>O. Ubbink and R. I. Issa, "A method for capturing sharp fluid interfaces on arbitrary meshes," *J. Comput. Phys.* **153**, 26–50 (1999).
- <sup>18</sup>H. Rusche, "Computational fluid dynamics of dispersed two-phase flows at high phase fractions," Ph.D. thesis (Imperial College London, 2003).
- <sup>19</sup>T. Holzmann, *Mathematics, Numerics, Derivations and OpenFOAM®* (Holzmann CFD, 2019).
- <sup>20</sup>I. V. Khalzov, D. Krotez, and R. Ségas (2023). "ISM-hydro and OpenFOAM: A quantitative comparison," Mendeley Data, V1, Dataset <https://doi.org/10.17632/x6cg77vw9s.1>